The electrical conductivity of solution-processed nanosheet networks

Adam G. Kelly, Domhnall O'Suilleabhain, Cian Gabbett and Jonathan N. Coleman ✉

Abstract | Solution-processed networks of 2D nanosheets are promising for a range of applications in the field of printed electronics. However, the electrical performance of these networks — represented, for example, by the mobility — is almost always inferior to that of the individual nanosheets. In this Review, we highlight the central role that the inter-sheet junctions play in determining the electrical characteristics of such networks. After briefly reviewing ink formulation and printing methods, we use a selection of electronic applications as examples to demonstrate the dependence of network conductivity on network morphology. We show the network morphology to be heavily influenced by the deposition method, the post-treatment regime and the nanosheet properties. In turn, the morphology of the network fundamentally determines the properties of the inter-sheet junctions, which, ultimately, control the electrical performance of the network. We use reported electrical data to show that three main conduction regimes exist: the network conductivity can be limited by the junctions, by a combination of junction and material properties or, very rarely, by the material properties. Using a meta-analysis of published data, we propose simple models relating network conductivity and mobility to the junction resistance.

2D materials have been intensively studied in recent years[1,2]. The field originated with the isolation of graphene, then expanded to hexagonal boron nitride and transition metal dichalcogenides (TMDs), before exploding to include thousands of 2D materials[3]. These materials have interesting electronic and optoelectronic properties that have led to a range of devices based on single nanosheets, including transistors[3–5], light-emitting diodes[6–8], photovoltaic devices[9,10], capacitors[11,12] and memory devices[13,14].

2D materials can be fabricated in large quantities as micrometre-sized nanosheets dispersed in liquids[15]. Such dispersions can be printed into thin films[16] suitable for applications[17] that range from energy storage to sensing and, of course, electronics. The possibility to incorporate 2D materials in solution-processed devices, combined with their electronic diversity, makes these materials ideal for printed electronics[18], a field of application where low-cost and large-area fabrication can be more important than exceptional device performance.

The key to the solution processing of 2D materials is liquid exfoliation, a set of processes by which layered materials can be converted to liquid-dispersed nanosheets[19]. Such dispersions are the basis of nanosheet inks that are easily deposited by a range of printing technologies to form nanosheet networks[17]. These networks consist of disordered arrays of nanosheets that are somewhat aligned in-plane, can cover large areas and display distinct properties, such as porosity and connectivity[20]. Network deposition by printing has been a crucial driver of device prototyping, as it offers versatility in device design, good reproducibility and the ability to form complex heterostructures composed of multiple nanosheet networks.

In-plane-aligned networks of nanosheets have a geometry well suited to thin-film formation. Unlike nanotube networks, adjacent nanosheets can interact conformally over large areas, leading to effective inter-sheet charge transfer. In contrast to nanoparticle arrays, the lack of dangling bonds on the nanosheet basal plane minimizes the need for passivation and reduces the propensity for charge trapping. The great diversity across the 2D family of materials enables the printing of conducting, semiconducting, dielectric and electrochemically active networks, which has led to the demonstration of a number of devices, including transistors[21,22], photodetectors[23,24], capacitors[25,26] and supercapacitors[27–29].

However, the performance of devices based on nanosheet networks is generally inferior to that of

School of Physics, CRANN and AMBER Research Centres, Trinity College Dublin, Dublin, Ireland.

✉*e-mail: colemaj@tcd.ie*

https://doi.org/10.1038/s41578-021-00386-w

devices using individual nanosheets[21]. This discrepancy in performance is believed to arise from reductions in carrier mobility associated with the transfer of charge across inter-sheet junctions. As in 0D[30] and 1D[31] systems, junctions can lead to parasitic resistances that can be significantly higher than the resistance of the individual constituents[32]. This effect can be highly inconsistent: the reported MoS_2 network conductivity varies by 10^5 among papers[21,23,33], presumably owing to variations in junction quality. Although improvements in specific devices have been achieved, there is comparatively little discussion on the fundamental role that inter-sheet junctions play in mediating the network properties. However, enough data are now available on nanosheet networks to draw useful inferences about the nature of the inter-sheet junctions and their impact on the electrical properties of network-based devices.

Several recent reviews have covered ink formulation and deposition techniques in detail, with some discussion of printed devices[19,34–37]. Here, we review the electrical properties of printed nanosheet networks, focusing on the effect of the inter-sheet junctions. We begin by briefly discussing solution-based exfoliation, ink formulation and printing methods. We then survey a selection of nanosheet-network devices, discussing how the morphology of such networks affects the electrical properties via inter-sheet junctions. Finally, we distil this information into a basic analysis of the conduction mechanisms that are present in these systems. In the interests of brevity, we focus on 2D materials produced by liquid-phase exfoliation or related methods and exclude devices based on graphene oxide, except where instructive.

Exfoliation and ink formulations

2D nanosheets can be liquid-exfoliated using many scalable techniques. Several industrial processes, including high-shear mixing[38–40], wet-jet milling[41,42] and microfluidization[43,44], have been used to exfoliate layered crystals, but the most common solution-based exfoliation methods are liquid-phase exfoliation (LPE) and electrochemical exfoliation. These techniques produce nanosheets with contrasting properties that can impact device performance.

Liquid-phase exfoliation

Through ultrasonication or high-shear exfoliation[15,19,45], layered crystals can be exfoliated in solution to yield polydisperse nanosheets in certain solvents, aqueous surfactants or polymeric solutions[15,46–49]. The strength of this technique lies in its ability to exfoliate a wide range of layered materials, including graphite, hexagonal boron nitride, metal chalcogenides and beyond[50]. Exfoliation involves the delamination and fragmentation of nanosheets from the bulk crystal (FIG. 1a) and yields nanosheets that are hundreds of nanometres in size and typically 1–20 layers thick[47,48,50]. Mechanistic studies have revealed that the average nanosheet length $\langle L_{NS} \rangle$ and the layer number $\langle N \rangle$ are coupled variables (FIG. 1b) related through nanosheet mechanics[50,51]. Liquid-exfoliated nanosheets are polydisperse, but can be size-selected by centrifugation (FIG. 1b) to give fractions with narrowed length and thickness distributions and increased monolayer yields[52]. The quality of the starting crystal can influence the electrical properties in the monolayer limit[53], with good-quality starting materials yielding relatively defect-free nanosheets with narrow photoluminescence linewidths[52].

Electrochemical exfoliation

Nanosheets can also be exfoliated by electrochemically intercalating ions into the bulk crystal to widen the inter-sheet distance (FIG. 1a). This strategy lowers the energetic cost of exfoliation, facilitating delamination immediately following intercalation[54] or during subsequent bath sonication[55]. Electrochemical exfoliation typically yields thin, large-area nanosheets, but often introduces basal-plane defects[55,56]. Lithium is a commonly used intercalant, but doping[57] or instigation of semiconducting-to-metallic phase transitions are common side effects[58,59]. Larger ions can avoid such transitions, but the exfoliation yield depends on both the intercalant size and the inter-planar spacing of the material being exfoliated[60]. The delamination of predominantly large-area, monolayer nanosheets is advantageous, as each nanosheet has approximately the same bandgap and can be highly flexible. However, because techniques such as inkjet printing have a limit on the maximum particle size[16], a subsequent ultrasonication step may be required to generate nanosheets small enough to print[16,61].

Ink refinement

Solution-based exfoliation yields dispersions that are easily converted to inks via rheological refinements[19,37,62]. To refine a dispersion into an ink, the nanosheets need to be size-optimized for a given deposition technique, and the solvent must be rheologically tuned to the material, deposition technique and substrate using additives such as polymeric binders, solvents and/or surfactants[17] (FIG. 1c). Although some solvents are usable without rheological tuning[16,17,23,25], they are often toxic, require high-temperature annealing, or need surface-energy modification for compatibility with a given substrate. Alcohols are desirable solvents owing to their low boiling point and low toxicity, but often need refinement using binary solvent blends[63,64] or polymeric stabilizers[64–68]. In addition, the transfer of the nanosheets from a solvent with a high boiling point such as *N*-methyl-2-pyrrolidone can be performed to ensure stability in an alcohol[21,27,69,70]. Water-based inks have also been reported, with the surface energy and viscosity tuned through surfactant and polymeric additives to create inks suitable for deposition by inkjet printing[26,27,61,62,71], screen printing[72–74] and spray coating[22,73,74].

For techniques such as screen or flexographic printing that require high-viscosity inks, the viscosity can be increased through the addition of polymers or high-viscosity solvents[66,74], or simply by increasing the nanosheet concentration[65,75]. Above a critical nanosheet concentration, the viscosity of the dispersion increases rapidly[76], allowing viscosity tunability while minimizing the quantity of additives. High nanosheet concentrations are often achieved using a single centrifugation step to remove only the largest unexfoliated particles,

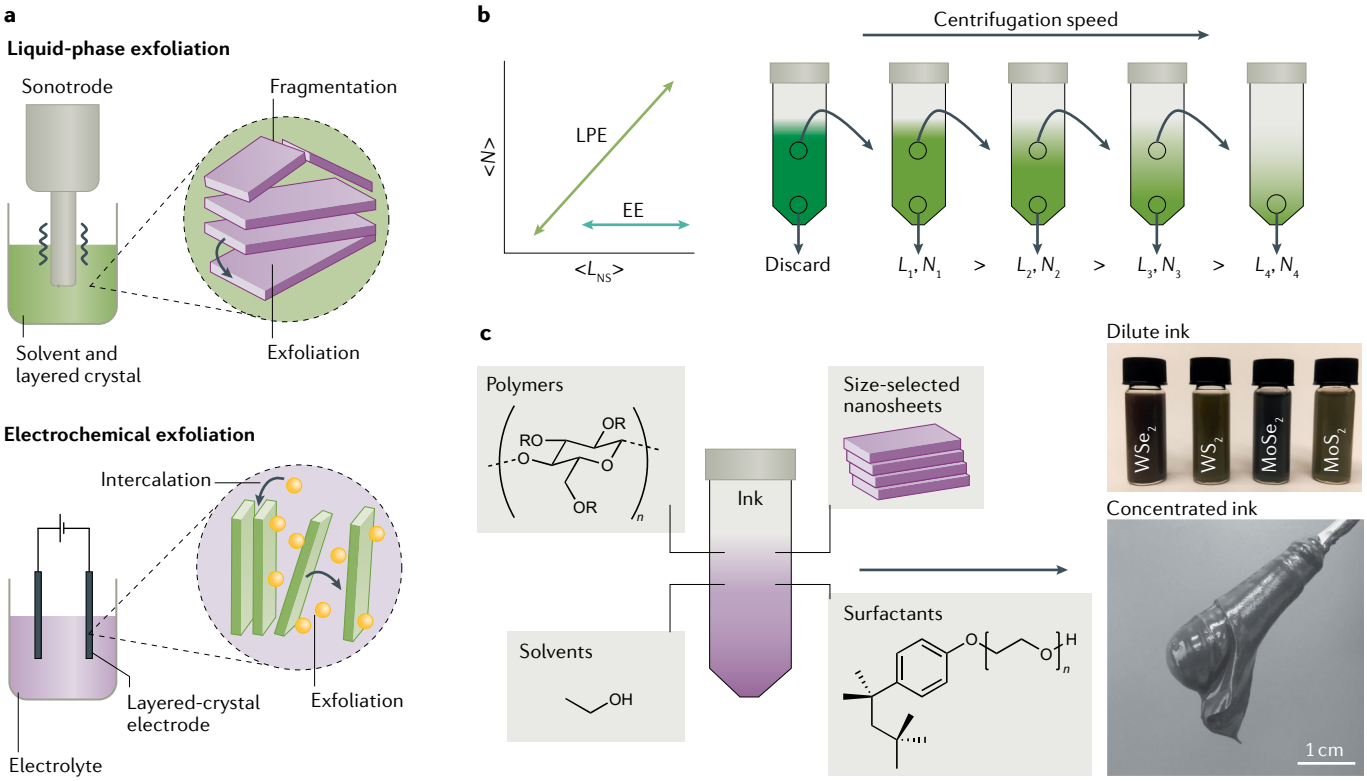

Fig. 1 | **Exfoliation and inks. a** | Schematics of liquid-phase exfoliation (LPE) and electrochemical exfoliation (EE). During LPE, the nanosheets are exfoliated and the basal planes are fragmented by ultrasound, whereas during EE, molecules are intercalated between the nanosheets, easing exfoliation. **b** | The average length $\langle L_{NS} \rangle$ and the layer number $\langle N \rangle$ of the exfoliated nanosheets are coupled for LPE and uncoupled for EE (left). To separate nanosheets of different sizes in a polydisperse suspension, liquid-cascade centrifugation can be used (right): successively increasing speeds draw a sediment with nanosheets of a given length and thickness to the end of the vial, leaving the supernatant containing smaller and thinner nanosheets, which can be isolated using a higher centrifugation speed. **c** | Once the nanosheets are size-selected for a given deposition method, an ink is prepared by tuning the rheology of the solvent (or solvent blend) using various ratios of polymers and/or surfactants. For non-contact deposition methods, a low-viscosity, dilute ink is typically required (with nanosheet concentrations of 1–3 g l^{-1}), whereas contact deposition methods require high-viscosity, concentrated inks, which are achieved using nanosheet concentrations higher than 30 g l^{-1} and/or high-viscosity solvents. Image of dilute ink reprinted with permission from REF.[21], AAAS; image of concentrated ink reprinted with permission from REF.[65], Wiley.

meaning these inks contain a wide distribution of nanosheet lengths and thicknesses[77,78]. Post-processing can be minimized for binder-free inks, but retaining a polymer within the printed network can result in greater network cohesion[40,77] and substrate adhesion[77], so the ink formulation should be selected with both deposition method and final application in mind.

Printing nanosheet networks

Advances in printed electronics have provided a wealth of techniques for printing nanosheet networks[17,19,79]. Here, we divide the printing methods into those that require concentrated (>30 g l^{-1}) and dilute (<5 g l^{-1}) inks, which broadly correspond to contact and non-contact deposition, respectively.

Contact deposition

The contact deposition techniques that have been reported tend to require medium-to-high-viscosity inks that are applied directly to the substrate. Screen printing[35,65,80], blade coating[45,67,81] and continuous roll-to-roll processes[82,83] have successfully used either stencil-based or intaglio patterning to create continuous networks in a single deposition. Owing to its low complexity and cost, much work has focused on screen printing, achieving pattern resolutions of ~100 µm (REF.[84]). The high-viscosity requirement saw early inks laden with polymeric binders, but recent work has moved towards binder-free inks in which high viscosities are reached with high-concentration inks (>50 g l^{-1})[74,85], reducing the need for high-temperature annealing. The resultant networks tend to be thick (>10 µm) and the interfaces between successive prints can be rough[78], which may preclude sequential layering of discrete materials. However, blade coating can be used to create networks with highly aligned nanosheets when the ink is optimized[81]. Although reports are few, gravure and flexographic processes offer high throughput at a higher resolution (down to 20 µm) and considerably lower thicknesses (~1 µm). A high-throughput process can require litre-scale volumes of ink[17], highlighting the importance of scalable exfoliation methods.

Non-contact deposition

Several non-contact techniques, including spray coating[17,21,75], inkjet printing[25,86,87] and aerosol-jet printing[64,71,88], have been harnessed to deposit low-viscosity, nanosheet-based inks. As each of these techniques is nozzle-based,

the ink concentration needs to be carefully optimized to prevent blockages, with most inks in the range of 1–3 g l^{-1}. In contrast to the blanket deposition of the spray coating method, inkjet and aerosol-jet printing are direct-write, low-waste processes with high resolution (feature sizes down to 10 µm), which makes them attractive for prototyping novel materials for which low masses are available. Aerosol-jet printing offers a wide tolerance in ink rheology and improved resolution compared with inkjet printing, but it is a relatively nascent technology. Conversely, inkjet printing has been the most frequently reported printing method, as the hardware and procedures have already been established for printed organic materials[89–91]. Other non-patternable, dilute-ink deposition methods, such as drop casting[92–94], spin coating[95–97], Langmuir–Blodgett deposition[33,98,99], layer-by-layer deposition[29,100] and liquid–liquid interface assembly[101], have also been reported, each giving a different network morphology.

There are several challenges associated with non-contact deposition processes. First, as droplets evaporate, the nanosheets are driven towards the droplet edge, resulting in non-uniform films (the coffee-ring effect)[102]. This effect can be counteracted by inducing surface tension gradients using surfactants[71] or binary solvents[103] to recirculate the internal flow, or by using a porous substrate where solvent penetration occurs much faster than evaporation or particle migration[104]. Second, the low ink concentration means the networks are rarely continuous and often poorly conductive after a single print, with pinholes evident even after several prints[23,25,26,71]. Although this issue can be addressed using multiple printing passes, the thickness can be smaller than 10 nm per pass[105], meaning many passes may be required to create a continuous network. Nonetheless, the identification and management of such challenges has enabled the realization of a multitude of printed nanosheet-network devices.

Nanosheet networks and their applications

When nanosheets are deposited on a substrate, they form networks consisting of disordered arrays of nanosheets with considerable porosity and some degree of in-plane alignment[74]. Within these networks, the nanosheets are connected via junctions at the locations where adjacent nanosheets are in close proximity, separated only by a narrow van der Waals gap. Importantly, this means that electrical conduction through the network is partially limited by the hopping or tunnelling of charge carriers across these junctions[106,107].

Although the charge transport mechanisms in these networks are not yet understood, temperature-dependent conductivity measurements have begun to reveal which transport regimes may be present. For example, magnetotransport measurements at various temperatures on MXene networks led to the identification of variable-range hopping between individual MXene sheets as the primary transport mechanism[106]. However, the field is relatively young, and comprehensive microscopic mechanistic studies are not widespread. As a result, as with nanotube and nanowire networks[108–112], conduction in nanosheet networks is usually analysed at a mesoscopic level via resistor networks, where resistances are assigned to the nanosheet and the junction[20,111].

In a network, the movement of a charge carrier within a nanosheet is always accompanied by a passage across a junction, such that the conductive path (highlighted in grey in FIG. 2a) can be considered as an arrangement of in-series pairs of resistances representing the nanosheet (R_{NS}) and the junction (R_J). This means the network resistance should depend on $R_J + R_{NS}$ (REFS[113,114]). The relative magnitude of R_{NS} and R_J then determines whether the nanosheet resistance or the junction resistance is the limiting factor for the network conductivity. Whereas the nanosheet resistance is a material-dependent property, the morphological details of the junction determine the effective inter-sheet resistance, which significantly impacts the network mobility.

The junction resistance has been explored using conductive atomic force microscopy to measure steps in resistance as the tip is moved across junctions between pairs of nanotubes[31,112,115] or nanosheets[32,116] (FIG. 2a, inset). Similarly, patterned electrodes have been used to directly compare internal nanowire or nanosheet resistances with the resistance across the inter-wire[108,117,118] or inter-sheet junction[119]. These studies all show a well-defined junction resistance that, for conducting nanomaterials, can be orders of magnitude larger than the intra-tube or intra-sheet resistance.

In addition to networks consisting of a single material, one can envisage heterostructure devices printed from combinations of conducting, semiconducting and insulating networks. The interface between discrete networks is of importance for such devices; for example, for photovoltaic applications, interfacial recombination losses can be significant[120,121].

Efficient electronic conduction within the network is usually key to device performance and is closely linked to the network morphology. In this section, we discuss some applications that demonstrate the importance of network structure, grouped according to the electronic characteristics of the active material.

Conductive networks

Graphene has been the focus of an enormous amount of application-based investigations. The reported applications typically require a reasonable conductivity, and much has been published on the use of graphene networks as static electrodes[23,25,71,122], flexible electrodes[123–125], transparent conductors[126,127], antennae[74,128], electromagnetic shields[129,130], supercapacitors[131,132], gas sensors[132–135] and biosensors[136–138]. However, the low density of states around the neutrality point limits the conductivity, owing to the relatively low carrier density (the conductivity of graphene networks is explored further in the following sections).

The exploration of metallic alternatives, such as VS_2 and VSe_2 (REFS[139–142]), and the 1-T polymorphs of some TMDs, such as MoS_2 (REFS[143–146]), has now begun in earnest, but it is the growing family of transition metal carbide and nitride ceramics, MXenes, that has seen the greatest amount of investigations[147,148]. MXenes show a network conductivity that far surpasses that of graphene[81,148,149], and has been exploited in applications

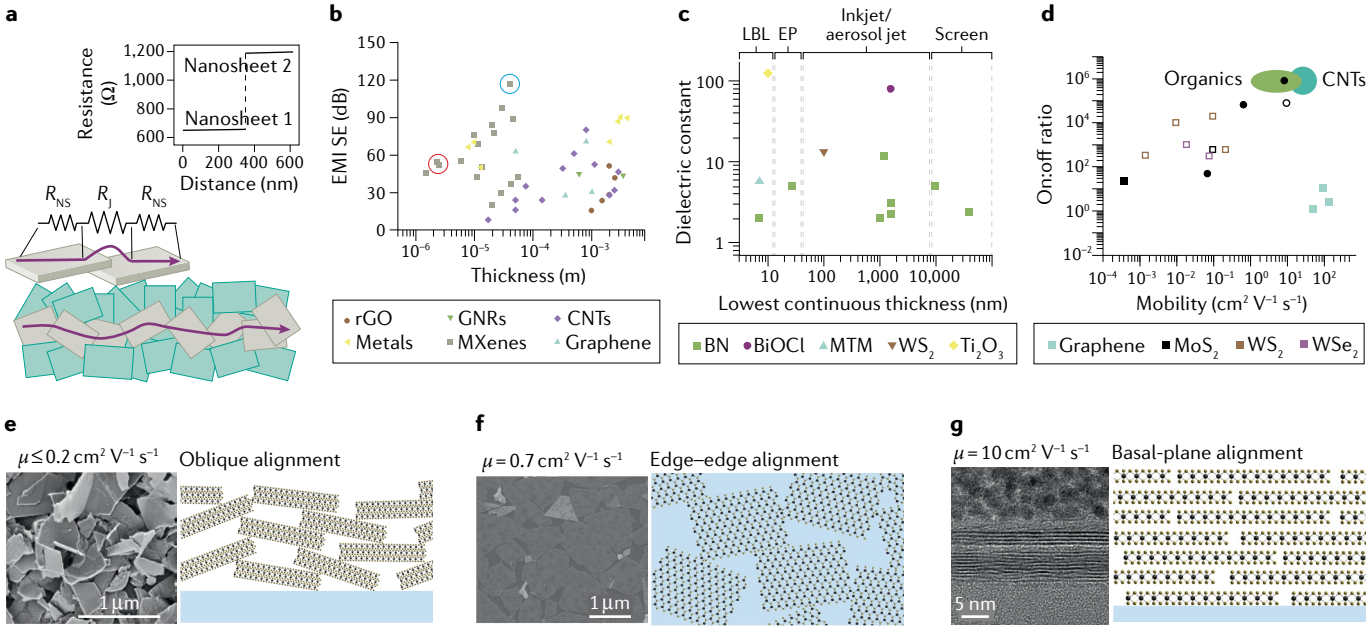

Fig. 2 | **Nanosheet-network properties. a** | A schematic of a nanosheet network. The purple line indicates the path of a charge carrier through the grey nanosheets, where it encounters series resistances caused by the nanosheets and the junctions. A conductive atomic force microscopy measurement showing a large step as the atomic force microscope tip crosses an inter-sheet junction (inset). **b** | The reported electromagnetic interference shielding effectiveness (EMI SE) for a range of nanomaterials and some common metals plotted against the shield thickness. The circles highlight values for a doctor-bladed MXene network showing a high in-plane alignment (red) and for a more porous system (blue), in which the porosity enhances the EMI SE. **c** | The dielectric constant of several insulating materials is plotted against the lowest thickness at which the nanosheet network is continuous (that is, pinhole-free). WS_2 is included for comparison. **d** | The on:off ratio versus mobility for several layered materials, with the approximate range for state-of-the-art carbon nanotube (CNT) networks and organic materials shown for reference. The square symbols are for liquid-phase-exfoliated materials and the circular symbols for electrochemically exfoliated materials. The open symbols are for electrolytically gated devices and the filled symbols for electrostatically gated devices. **e** | An obliquely aligned nanosheet network of liquid-phase-exfoliated WSe_2 nanosheets. **f** | An edge–edge-aligned network of electrochemically exfoliated MoS_2 nanosheets. **g** | A basal-plane-aligned network of electrochemically exfoliated MoS_2 nanosheets. μ, mobility; BN, boron nitride; EP, electrophoretic; GNR, graphene nanoribbon; LBL, layer-by-layer; MTM, montmorillonite; rGO, reduced graphene oxide. Panel **a** reprinted with permission from REF.[32], ACS; panel **e** left reprinted with permission from REF.[21], AAAS; panel **f** reprinted from REF.[101], CC BY 4.0; panel **g** reprinted from REF.[58], Springer Nature Limited and schematics in panels **e**, **f** and **g** courtesy of Katarzyna Stachura.

such as transparent electrodes and electromagnetic interference (EMI) shielding[150–154].

Example application: EMI shielding. EMI shielding is a particularly useful application for comparing conductive networks, as the shielding effectiveness includes reflective and absorptive components, which both depend on network conductivity[155]. The EMI shielding effectiveness for a range of materials and thicknesses is plotted in FIG. 2b. A high EMI shielding effectiveness at low thickness is desirable for reasons of weight and cost (Supplementary Table 1). 2D systems are vastly superior to most 1D systems at low thickness and, although carbon-based shields can outperform some common metals, MXenes now, in turn, outperform them[81,151,154–157].

Networks of highly aligned MXenes show good shielding effectiveness at very low network thickness, partly due to high conductivities. For example, networks of large, thin MXene nanosheets with high in-plane alignment[81] (FIG. 2b, point in the red circle) lead to a large interfacial area that minimizes the junction resistance, yielding a conductivity larger than $10^6\ S\ m^{-1}$. Beyond conductivity, microstructural effects associated with porosity (FIG. 2b, point in the blue circle) have been shown[158] to yield EMI shielding effectivenesses far beyond those predicted by theory.

Dielectric networks

Although most papers on nanosheet networks focus on electrical rather than dielectric properties, insulating components are a critical part of any electronic architecture. Reports on dielectric networks began with boron nitride, but networks composed of montmorillonite[159], titania[100] and bismuth oxychloride[160] nanosheets have also been explored. Such networks have enabled the development of vertical heterostructures such as parallel-plate capacitors[25,160] and field-effect transistors[26,88]. Several studies have used the capacitor structure as a test bed for probing dielectric networks.

Example application: capacitors. A number of reports have investigated printed capacitors consisting of vertically stacked heterostructures, such as graphene/boron nitride/graphene[25,161,162]. High areal capacitances are achieved by maximizing the dielectric constant (a material property) and minimizing the dielectric thickness (a network property). To avoid pinholes, spatial continuity in thin networks is crucial[23,163]. The lowest thickness

at which a continuous (pinhole-free) dielectric network is formed for several materials is shown in FIG. 2c, along with their respective dielectric constants (Supplementary Table 2). The lowest continuous network thickness clearly depends on the deposition technique and varies across four orders of magnitude. Screen printing creates continuous networks more than 10 μm thick[164], whereas inkjet printing[26,164], aerosol-jet printing[88] and spray coating[25,88] create continuous networks with a thickness of 1–2 μm. The thinnest networks are those created through layer-by-layer[159,160,165] or electrophoretic[166] deposition, where continuity can be achieved at thicknesses smaller than 20 nm. Although these methods do not allow patterning, the demonstration that continuous networks can be achieved at such low thicknesses is important.

That the same material can yield discontinuous networks with one deposition method yet continuous networks with another highlights the importance of network morphology. The layer-by-layer technique compacts the nanosheets into a tightly tiled network with low porosity. Forming such thin pinhole-free networks with non-contact deposition is far more challenging, as using dilute inks leads to nanosheet migration[70,71,166,167] and redispersion can occur when sequential layers are deposited[71]. The lowest continuous thickness for direct-write methods clusters between 1 and 2 μm, higher than that achievable with electrophoretic or layer-by-layer deposition. Interestingly, identical ink formulation and deposition methods yield continuous network thicknesses of ~1 μm for boron nitride[26] but ~100 nm for WS_2 (REF.[71]), indicating that as-yet unidentified factors may play a role. The degree to which the network morphology is tunable within a given deposition method remains an open question.

Semiconducting networks

A key selling point of the layered-crystal materials family is its diversity, which provides access to a wide range of semiconductors, without the purification or selectivity steps needed for 0D and 1D materials[168]. Layered semiconductors are well suited for optoelectronic applications, as they possess bandgaps ranging from 0.3 eV for black phosphorus[169] to ~3 eV for MoO_3 (REF.[170]). Networks created from semiconducting nanosheets typically show in-plane mobilities in the range 10^{-2}–10 $cm^2 V^{-1} s^{-1}$, which have allowed them to be utilized in photodetectors[23,171,172], transistors[21,24,101] and memory devices[22,71]. LPE-based TMDs such as MoS_2 and WS_2 have also been utilized as the light-absorbing[173–175] and hole transport layers in photovoltaic applications[173–175], with WS_2 demonstrating a performance similar to that of poly(3,4-ethylenedioxythiophene) polystyrene sulfonate (PEDOT:PSS)[176,177]. For applications such as photovoltaics, the out-of-plane conductivity needs to be evaluated, as it is expected to be much lower than the in-plane conductivity[20]. For example, in liquid-phase-exfoliated MoS_2 films, in-plane[33] conductivities of ~10^{-6} S m^{-1} can be contrasted with out-of-plane[99] values of ~10^{-10} S m^{-1}.

Example application: thin-film transistors. The demonstration of a transistor based on a printed nanosheet network was always an important goal, but effectively modulating the current initially proved challenging. To be competitive with organic and carbon nanotube (CNT) devices[178,179], a printed transistor should have on:off ratios bigger than 10^6, with a mobility of at least 10 $cm^2 V^{-1} s^{-1}$. The on:off ratio versus network mobility for a range of printed nanosheet networks is shown in FIG. 2d, with the range of values for state-of-the-art organic and CNT networks shown for reference (Supplementary Table 3). Semiconducting TMDs display a broad range of on:off ratios and mobilities[21,22,101,180–182]. Interestingly, networks composed of liquid-phase-exfoliated nanosheets tend to show lower mobilities and on:off ratios than those created by electrochemical exfoliation. Although there have been several demonstrations of printed graphene transistors[26,27,62,64] with mobilities up to 150 $cm^2 V^{-1} s^{-1}$, these devices are naturally impeded by the low on:off ratios associated with semimetals.

Mobility and conduction regimes. It is becoming clear that the variation in network mobility shown in FIG. 2d is strongly linked to network morphology. For example, FIG. 2e shows a scanning electron microscope image of a spray-coated, liquid-phase-exfoliated TMD network[21]. Here, the nanosheets were size-selected to remove thin nanosheets and reduce the variation in local bandgaps across the network. This procedure leads to thick ($<t_{NS}>$~12 nm) and rigid nanosheets that, once deposited into a network, form a jammed system[183] of obliquely aligned nanosheets with high porosity (P_{Net}~0.5), resulting in point-like contacts between the nanosheets. The overlap area between the basal planes is, therefore, small, generating high junction resistances and low mobilities of ~0.1 $cm^2 V^{-1} s^{-1}$.

Such low network mobilities mean thick films are needed to yield appreciable currents, which results in low on:off ratios, as the current is only modulated in a small region near the semiconductor–dielectric interface[172]. One solution to this problem is to use a liquid electrolyte that penetrates the porous free volume of the network to electrochemically gate all parts of the channel[21,22,64,172,181]. Although this approach overcomes the problems associated with high junction resistances, it would be preferable to enhance the network mobility by changing the nature of the junctions.

Improvements in the network morphology have been delivered in two recent reports using electrochemical exfoliation coupled with different network formation techniques. The first paper[101] presented a predominantly bilayer ($<t_{NS}>$~2 nm) MoS_2 network, obtained by using the surface-energy gradient along a liquid–liquid interface to compact the nanosheets into an edge-aligned network (FIG. 2f). Although the edge–edge interfaces between the nanosheets are small in area, the dense packing of the nanosheets (~90%) appears to reduce the junction resistance sufficiently to allow the electrostatic gating of the network, resulting in a network mobility of 0.7 $cm^2 V^{-1} s^{-1}$.

In the second paper[58], nanosheet alignment was obtained by spin-coating thin electrochemically exfoliated nanosheets ($<t_{NS}>$~3.8 nm) to create highly aligned networks (FIG. 2g). Here, a high basal-plane alignment leads to large-area junctions where adjacent nanosheets

conform to each other, significantly enhancing the inter-sheet charge transfer. This leads to network mobilities of ~10 $cm^2 V^{-1} s^{-1}$, close to those measured for the individual nanosheets (11 $cm^2 V^{-1} s^{-1}$), suggesting that the junction resistance has been reduced to the point where electronic conduction is determined by the properties of the nanosheets, rather than those of the junctions. Following a related protocol[184], it was confirmed that networks of large and thin MoS_2 nanosheets ($<t_{NS}>$~2.3 nm) can show mobilities of 10 $cm^2 V^{-1} s^{-1}$. It is worth noting that, in both works[58,184], chemical post-treatments were applied to the networks, which could affect the junction properties. However, printed networks of thin, electrochemically exfoliated $NbSe_2$ nanosheets created without a chemical post-treatment step were recently demonstrated[119], yielding large-area, conformal junctions and very low junction resistances of less than 500 Ω, showing that chemical treatment is not required to achieve low junction resistance.

These developments allow us to propose a number of conduction regimes: junction-limited conduction (where $R_J \gg R_{NS}$), material-limited conduction (where $R_J \ll R_{NS}$) and a possible combination of both (where $R_J \sim R_{NS}$). As the networks in FIG. 2e,f show mobilities well below those of the nanosheets, they are at least partially limited by junctions, whereas the network in FIG. 2g is probably in the material-limited regime. Drawing distinctions between these conduction regimes is important for device reproducibility and optimization.

Factors influencing inter-sheet junctions

The variation of mobility described above shows the impact of the network morphology on the conductivity of nanosheet networks. In this section, we explore the relationship between the network morphology and conductivity by examining data for a range of graphene networks.

The evolution of graphene network conductivities obtained over time for the two most frequently reported deposition methods, inkjet printing and screen printing, is shown in FIG. 3a (Supplementary Table 4). Other methods, such as blade coating[45,82,185], aerosol-jet printing[40,64,186], filtration[38,187], spin coating[96,98] and gravure[83,96,188], have also been used to deposit to graphene, but the data are too sparse to draw generalized conclusions. However, inks formulated for screen printing are very similar to those used in blade coating and flexographic and gravure printing, and often result in conductivities in a similar range (~10^4 S m^{-1})[45,82,83,189]. Although it is clear that network conductivities have improved over time, trending towards the graphitic basal-plane conductivity (~10^6 S m^{-1})[190], there is a broad distribution of values, ranging from 10^2 to 10^5 S m^{-1}. In addition, the screen-printed networks cluster higher in conductivity, with a median value of 4.3×10^4 S m^{-1}, than the inkjet-printed networks, with a median conductivity of 5.5×10^3 S m^{-1}.

One source of this spread in conductivities is the fact that different inks are used for different deposition

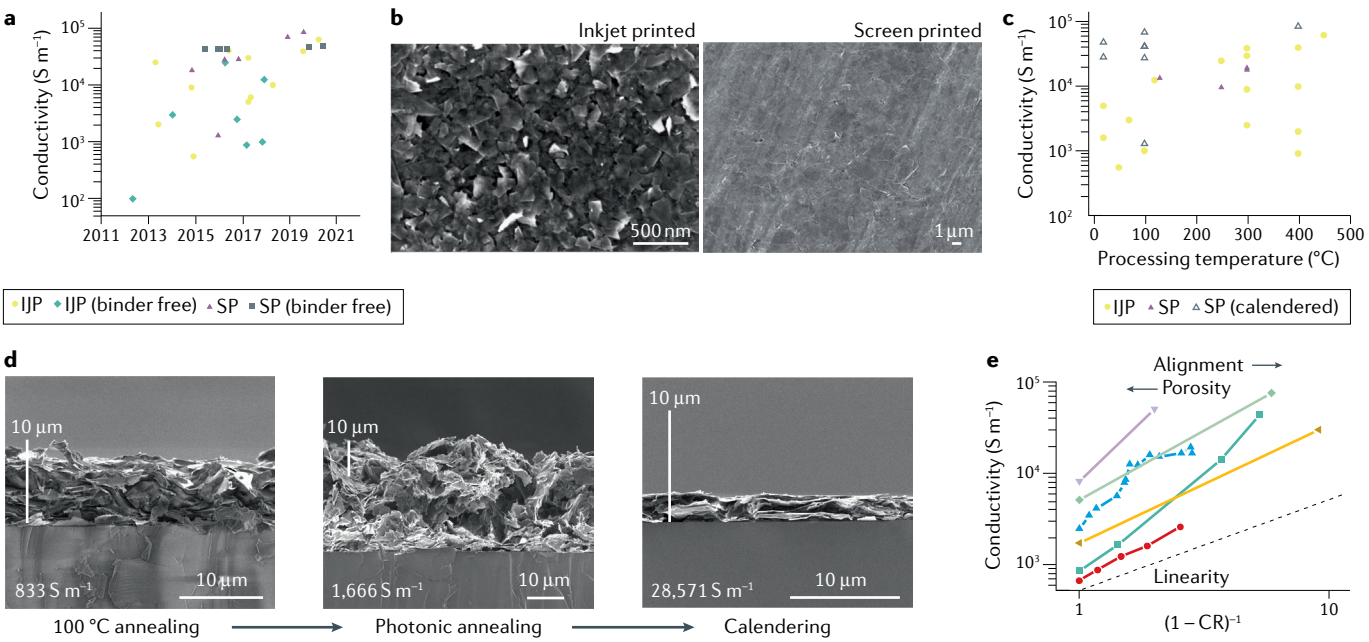

Fig. 3 | **Network morphology. a** | The evolution of network conductivity over time for inkjet-printed (IJP) and screen-printed (SP) networks of graphene. The diamond and square symbols indicate inks that are created without a polymeric binder. IJP data from REFS[16,23,27,61,62,68–70,72,105,185,191,248–253], SP data from REFS[65,66,71,74,77–79,85,128,200,254,255] (Supplementary Table 4). **b** | Scanning electron microscope images of IJP[23] and SP[85] networks showing visible differences in porosity. The SP network has been calendered. **c** | The conductivity data from panel **a** shown against processing temperature. The open symbols represent SP networks that have also been calendered. **d** | A SP graphene network after thermal annealing at 100 °C, then photonic annealing and, finally, calendering; the resulting conductivities are annotated on each image. **e** | Network conductivity plotted against $(1 - CR)^{-1}$, where CR is the compression ratio, and linearity would imply that the reduction in porosity is the primary factor that causes a conductivity increase upon compression. Data sources: dark green squares, REF.[200]; red circles, REF.[199]; yellow triangles, REF.[185]; light green diamonds, REF.[77]; blue triangles, REF.[20]; lilac triangles, REF.[74]. Panel **b** left reprinted with permission from REF.[23], RSC; panel **b** right reprinted with permission from REF.[85], AIP; and panel **d** reprinted with permission from REF.[185], Wiley.

techniques: inkjet-printable inks are typically dilute (<3 g l^{-1})[20,70,191], with nanosheet lengths smaller than 400 nm (REFS[23,25,71]), whereas screen-printable inks are high-loading (>50 g l^{-1})[61,79], have a broad length distribution and often include a polymer binder[77]. Binder-free inks have been developed for both deposition techniques[23,27,74,85] to avoid annealing and minimize residuals in the final networks. Although a lack of residuals in the printed networks should result in a higher conductivity, the conductivity is not maximized for such inks (diamond and square symbols in FIG. 3a), meaning both ink optimization and post-processing are necessary to achieve high-performance networks.

Although the network morphology is affected by the deposition technique, this effect is difficult to evaluate because most as-printed networks undergo some post-processing that improves the network characteristics by modifying its morphology. One significant difference in deposition techniques is the deposited mass; the low droplet volume in inkjet printing creates networks that are typically tens of nanometres thick, whereas screen-printed networks tend to be tens of micrometres thick. However, the fact that the conductivities of inkjet-printed and screen-printed inks have begun to overlap implies that combining an optimized ink formulation with post-treatment can alleviate unwanted deposition effects. Different processing routes typically result in visible differences in the final networks: FIG. 3b shows a porous inkjet-printed network with a relatively low conductivity (~3,000 S m^{-1})[23] alongside a calendered (compressed) screen-printed network with a relatively high conductivity (~43,000 S m^{-1})[85]. Whereas the nanosheets are distinct in the inkjet-printed network, they coalesce under the compression of the screen-printed network, which leaves them less distinguishable.

The continuous increase in conductivity shown in FIG. 3a has largely been achieved through post-processing techniques and tailoring of the nanosheet dimensions. We discuss such techniques and their effect on network morphology below.

Post-processing: thermal annealing

Thermal annealing is the most common post-processing technique and is predominately used to remove volatile elements and polymeric additives from the network. FIGURE 3c displays the conductivity data from FIG. 3a plotted versus the samples' processing temperatures (Supplementary Table 4). It is clear that inkjet-printed networks benefit considerably from thermal treatments, albeit at temperatures well above the glass transition temperature of flexible substrates (for example, polyethylene terephthalate has a glass transition temperature of around 70 °C)[192]. When annealing is the only post-treatment, a temperature higher than 250 °C is required to maximize conductivity. However, similar conductivities can be achieved at low temperature (<100 °C) in screen-printed networks that are subsequently calendered.

Thermal annealing not only volatilizes residual solvent (or surfactant) but, at elevated temperatures, can also decompose ink-stabilizing polymers. Although some polymers can dope nanosheets[105,193], their inclusion in a network is generally detrimental because they sterically separate the nanosheets. The removal of polymers has a number of beneficial effects: it causes a collapse in the network structure[68], reducing porosity; it allows the nanosheets to come into more intimate contact; and the resultant carbonization leaves a residue that may aid inter-sheet charge transfer under certain conditions[40].

Although the treatment of graphene can reach at least 450 °C without altering the material, TMDs are far more thermally sensitive. When MoS_2 is annealed at more than 200 °C in the presence of oxygen, *p*-type doping can occur[194], while beyond 300 °C, significant oxidation can convert the material to MoO_3 (REFS[194,195]). These problems may limit even moderate annealing as a useful method for improving conduction in sulfur-based TMD networks.

Post-processing: photonic annealing

It is important to be able to print on flexible substrates, such as polyethylene terephthalate or paper, which are incompatible with high-temperature annealing. To address this issue, photonic annealing has been investigated, often for binder-based inks[128,185,195–197]. This technique applies a series of light pulses to the nanosheet network, causing a rapid increase in local temperature (up to 500 °C)[128] that can decompose and volatilize organics, yet, leave the substrate intact.

Photonic annealing has shown good success in removing polymers and solvents from graphene networks, resulting in increases in either the conductivity[185] or sheet conductance[185,197]. However, the rapid volatilization has significant repercussions on the network morphology. Increases in network thickness of up to a factor of 2.5 after photonic annealing were reported[185,196,198] (FIG. 3d). This thickness increase is the consequence of an increase in porosity, which, in turn, dramatically affects the morphology[197,198]. This is in contrast to thermal annealing, where polymeric decomposition leads to a decrease in network thickness[68,198]. However, the rapid volatilization from photonic annealing may induce a more complete removal of a given binder compared with thermal annealing.

The removal of residual dopants and the changes in morphology mean that both carrier density and network mobility are altered by the photonic treatment, so it is interesting to note that, despite the network becoming more porous, the conductivity can still increase by more than a factor of two (FIG. 3d). That an increase in conductivity can be achieved despite a large increase in porosity is a counter-intuitive observation; as the quantity of nanosheets is ostensibly the same before and after treatment, this conductivity increase can only occur through a large decrease in network resistance, which must be due to either a reduction in junction resistance or increases in carrier density.

Post-processing: calendering

Improvements in the conductivity are also achievable at room temperature by compressing, or calendering, a network. Network compression produces a number of effects that can increase the network conductivity. First, the reduction in porosity following compression

increases the fraction of the film volume that carries current. Second, compression typically improves the degree of nanosheet alignment, which can also enhance in-plane conduction. A recent study demonstrated that enhancing in-plane nanosheet alignment increases the conductivity anisotropy often observed in nanosheet networks[20]. On compression, the in-plane/out-of-plane conductivity ratio can increase from ~10 to >1,000 (with a theoretical maximum of $(L_{NS}/t_{NS})^2$), showing that nanosheet orientation must play a distinct role in determining conductivity. Third, compression can increase nanosheet connectivity[20] (a measure of how many nearest neighbours a nanosheet has) and might even reduce junction resistance if adjacent nanosheets become highly aligned.

Calendering has been applied to screen-printed networks, where over tenfold improvements in conductivity have been reported[20,77,79,85,196,199]. Many of these networks are subsequently annealed at ~100 °C, meaning that ink residuals remain unless binder-free inks are used[74,79,85]. It has been suggested that room-temperature calendering can displace some residual surfactants from the networks, forgoing the need to anneal entirely[74]. The majority of reports apply calendering to screen-printed networks, but a spray-coated graphene network with an initial thickness of ~10 μm survived calendering without being destroyed[74]. Calendering has also been used to counteract the porosity increase caused by photonic annealing: the morphology of the photonically annealed network in FIG. 3d was improved with a calendering step that compressed the network by 89%, resulting in a conductivity of ~28,000 S m^{-1} (REF.[185]). However, a combination of photonic annealing and subsequent calendering still does not improve the network conductivity beyond the values obtained in some reports that used calendering alone (with values of 71,300 S m^{-1} in REF.[79] and 88,100 S m^{-1} in REF.[77]).

For screen-printed networks, the compression ratio ($CR = (t_0 - t)/t_0$, related to the fractional thickness change upon calendaring, where t_0 is the initial thickness) is typically higher than 50%, with some networks showing a CR > 80%. For example, a compression ratio of 81% that increased the conductivity from 830 S m^{-1} to 43,000 S m^{-1} was reported[200]. The compression ratio can also be expressed as $CR = (P_0 - P)/(1 - P)$, meaning the highest ratios are achieved when the initial porosity (P_0) is very high and the final porosity (P) is very low.

As indicated above, the compression of a network affects the conductivity through three primary effects: porosity reduction, improved nanosheet alignment and junction or connectivity modification. However, it is not currently known which effect is the most important. To make a basic assessment of these properties, we assume that pore annihilation is the dominant effect, meaning the network resistance (R_{Net}) remains constant, while the conductivity is modified via changes in network thickness. For a network with electrode spacing l and width w, the conductivity is $\sigma_{Net} = l/(R_{Net}wt)$. The network thickness after compression is given by $t = t_0(1 - CR)$, implying that the conductivity should scale as $\sigma_{Net} \propto 1/(1 - CR)$ when pore annihilation is dominant. In FIG. 3e, the network conductivities extracted from REFS[20,74,77,185,199,200] are plotted versus $1/(1 - CR)$, with linearity indicated by the dashed line. The data of REF.[199] (red circles), REF.[185] (yellow triangles) and REF.[77] (light green diamonds) are approximately linear, implying that a reduction in porosity is the dominant effect of calendering in these studies. The conductivity improves because the reduction in porosity means there is less free volume in the network that does not carry current. However, the data of REF.[200] (dark green squares) and REF.[74] (lilac triangles) are clearly superlinear, suggesting they cannot be explained by porosity reduction alone. Similarly, the data of REF.[20] (blue triangles) are superlinear at low porosity, owing to the effect of compression on network connectivity. These results suggest that nanosheet alignment and/or junction modification can play a significant role, although further isolating the effects of each factor will be challenging.

Nanosheet dimensions

Although it has not been qualitatively understood, some dependence of conductivity on nanosheet size has been reported for graphene oxide[201,202], graphene[62,74] and WS_2 (REF.[22]). A common axiom is that larger sheets form conductive paths with fewer junctions, resulting in higher network conductivity, as seen in CNT networks[203]. However, this may be an oversimplification. The conductivity of inkjet-printed and screen-printed networks for which length is reported is shown in FIG. 4a (Supplementary Table 4). No obvious trend exists to correlate conductivity with nanosheet length. However, one key element stands out: the highest conductivities can be achieved with either large or small nanosheets. This means that, whereas nanosheet length may be a relevant variable, the quality of the junctions appears to be more important than their quantity, at least for graphene.

As the bandgap of semiconducting nanosheets often depends on the number of layers[204], the nanosheet thickness should affect electronic conduction. Semiconducting networks fabricated from nanosheets with a range of thicknesses can contain a range of local bandgaps. Spatial bandgap uniformity has been shown to be important in CNT networks to minimize the inter-tube barriers that arise from conduction sub-band offsets and to avoid trapping[204,205]. One technique to homogenize the energetic landscape of a nanosheet network is to remove the thin, variable-bandgap nanosheets by centrifugation, leaving only nanosheets thick enough to display bulk properties[21,33,168]. However, this strategy yields a network containing thick, rigid nanosheets, which can limit the network mobility (FIG. 2e). For conductive nanosheets, it has been shown[62] that the mobility of a graphene network scales inversely with the nanosheet thickness (FIG. 4b). The mobility declines from 10–50 cm^2 V^{-1} s^{-1} when the graphene is predominantly monolayer to ~1 cm^2 V^{-1} s^{-1} when the nanosheets are ~6 nm thick.

It is not usually appreciated that the mechanical properties of the nanosheets must also be considered. To form an inter-sheet junction where the inter-sheet distance is minimized, a given nanosheet must be able to easily conform to those underneath. Although this process is driven by van der Waals interactions, the ability to conform is governed by the bending rigidity D, which is a measure of the energetic cost of bending

a platelet to a given curvature[206]. The ultra-thin nature of 2D nanosheets means monolayers can be very flexible; single layers of graphene (D~1.5 eV)[207] have been described as "more reminiscent of a liquid than a solid"[208], and TMD monolayers are only slightly stiffer (D~6–12 eV)[209]. As a result, thin nanosheets are highly conformable, and even multilayer nanosheets show excellent conformity[210,211] (FIG. 4c,d). This observation is supported by data on junctions of bilayer and trilayer $NbSe_2$ nanosheets, which form large-area, conformal junctions with $R_j < 500\,\Omega$ (REF.[119]). However, the bending rigidity increases rapidly with nanosheet thickness, t_{NS}, at a rate between the monolithic ($\sim t^3_{NS}$)[207,212] and stacked ($\sim t_{NS}$)[211] limits. Thus, above some critical thickness, multilayer nanosheets display values of D too high to allow the formation of low-resistance, conformal junctions.

This thickness dependence is illustrated in FIG. 4e, where bending rigidity data for various materials are plotted as a function of nanosheet thickness[213–217]. Considering the D versus t_{NS} data for MoS_2 of REF.[213] (green triangles), the electrochemically exfoliated MoS_2 nanosheets described in REF.[58] (light grey dashed line and FIG. 2g, $\langle t_{NS}\rangle$~3.8 nm) should have $D \sim 10^4$ eV, which must be low enough to allow conformal junctions. However, the liquid-phase-exfoliated MoS_2 nanosheets described in REF.[21] (dark grey dashed line and FIG. 2e, $\langle t_{NS}\rangle$~10 nm) have $D \sim 10^5$ eV, which must be too high for conformal junctions to form. Thus, the critical value of D above which conformal contacts can no longer occur is expected to be somewhere between 10^4 and 10^5 eV. To assess the validity of this observation, we reformulate the model presented in REF.[211] to show that a nanosheet of length L_{NS} can conform to two other nanosheets arranged at a relative angle of θ once $D < \gamma L^2_{NS}/4\theta^2$, where γ is the inter-nanosheet adhesion energy (Supplementary Information). Taking $L_{NS} = 300$ nm, $\gamma = 70$ mJ m^{-2} (typical values for liquid-phase-exfoliated MoS_2)[218] and an arbitrary bending angle of 30°, this simple model gives a limiting value of $D \sim 3.5 \times 10^4$ eV, in excellent agreement with the discussion above. Further analysis (Supplementary Information) shows that, for MoS_2, conformal, low-resistance junctions form once $L_{NS}/t_{NS} > 40$.

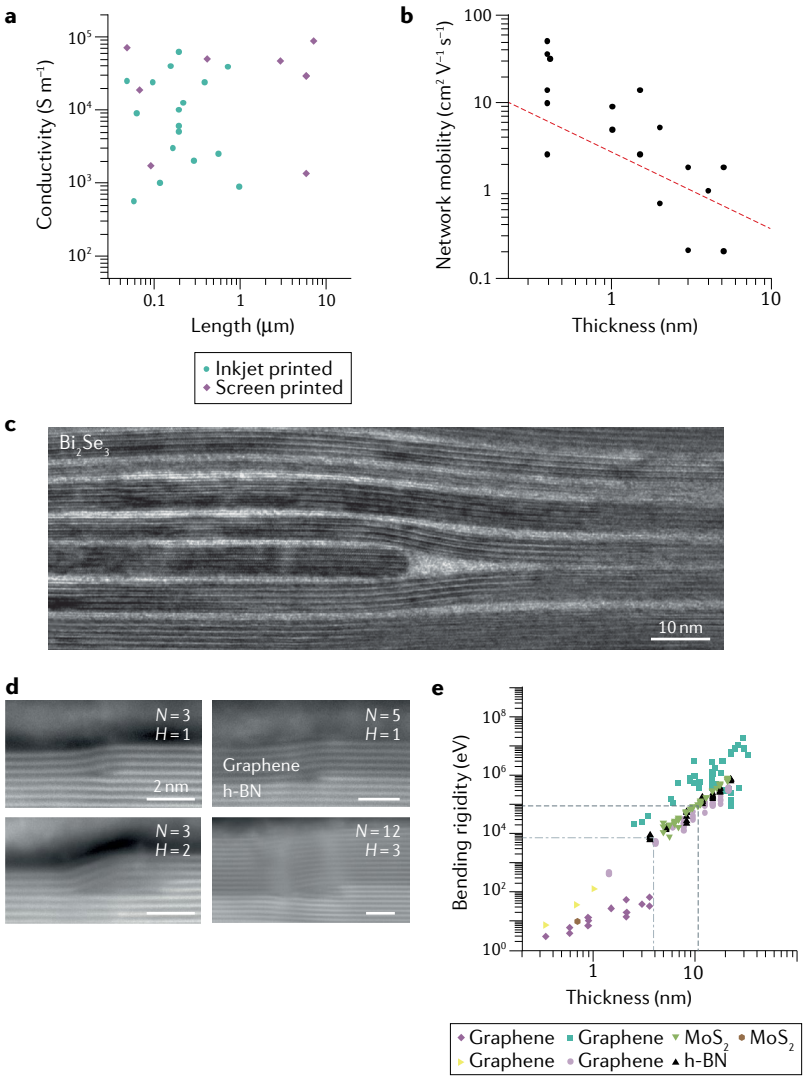

Fig. 4 | **Nanosheet dimensions. a** | The conductivity of various inkjet-printed and screen-printed graphene networks against the reported length of the nanosheets. No clear trend can be seen. **b** | The mobility of a graphene network against the thickness of the graphene nanosheets; the data points are from REF.[62]. The fit is to Eq. 3 with a junction resistance of 1 MΩ. **c** | A cross section of a network of spin-coated Bi_2Se_3 nanosheets. The nanosheets show excellent conformity, despite being few-layer thick. **d** | Cross sections of graphene nanosheets of various thickness (N layers) lying flush across a basal terrace of hexagonal boron nitride (h-BN) with steps of H layers. **e** | The bending rigidity for a range of materials versus their respective nanosheet thickness. The light and dark grey dashed lines indicate the thickness of the MoS_2 nanosheets reported in REF.[58] and REF.[21], respectively, and their approximate bending rigidity, estimated using the MoS_2 trend reported in REF.[213] (green triangles). Data sources: yellow triangles, REF.[214]; blue squares, REF.[213]; lilac circles, REF.[213]; purple diamonds, REF.[211]; black triangles, REF.[213]; green triangles, REF.[213] brown hexagons, REF.[217]. Panel **b** adapted with permission from REF.[62], Elsevier; panel **c** reprinted with permission from REF.[210], ACS; and panel **d** reprinted from REF.[211], Springer Nature Limited.

Network conduction mechanisms

A deeper understanding of the electronic conduction mechanisms present in nanosheet networks can be found via meta-analysis of published data. Electronic conduction in individual nanosheets is often analysed via electrode-limited models[219,220] (such as Schottky emission), which describe the electrode–material interface. However, nanosheet networks tend to be fabricated using widely spaced electrodes, leading to large network resistances. For example, the network resistance was shown[22,221] to be orders of magnitude larger than the electrode–network contact resistance, so long as the electrode spacing was greater than 10–20 μm. Systems with widely spaced electrodes tend to be bulk-limited[219], making it more appropriate to consider models based on the electrical properties of the network itself.

Network conductivities, mobilities and carrier densities

Because most reported devices are at least partially limited by inter-sheet junctions, they tend to display network mobilities that are significantly lower than the mobility of an individual nanosheet[21]. This can be illustrated by plotting the network conductivity (σ_{Net}) versus the network carrier density (n_{Net}, calculated from $n_{Net} = \sigma_{Net}/e\mu_{Net}$), as shown in FIG. 5a for the limited number of systems for which network

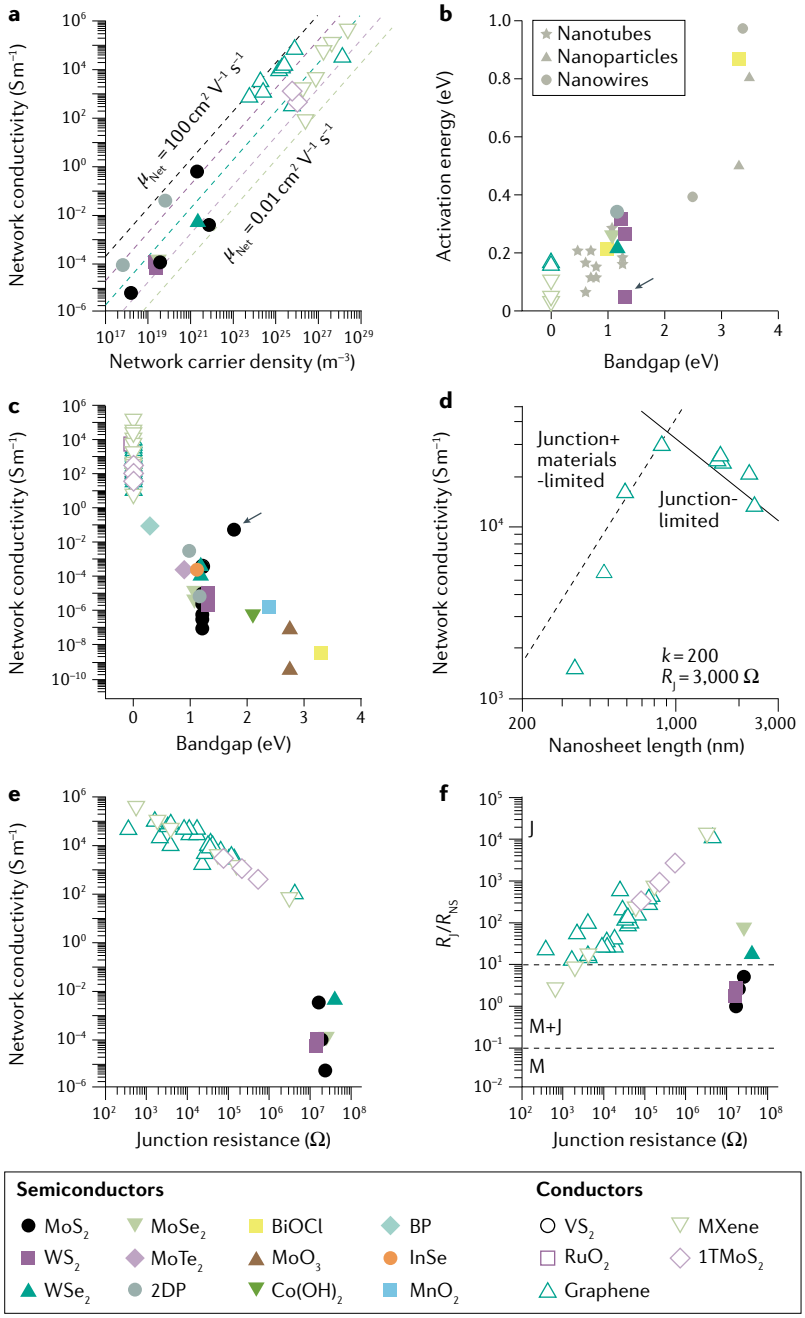

Fig. 5 | **Summary of electrical properties of nanosheet networks extracted from the literature. a** | Network conductivity plotted versus network carrier density for the subset of networks for which both quantities are known. The dashed lines represent the following network mobility values: 0.01, 0.1, 1, 10 and 100 $cm^2 V^{-1} s^{-1}$. **b** | Activation energy versus bandgap for networks that display an Arrhenius-like dependence of conductivity on temperature. For comparison, we include data for networks of carbon nanotubes[168,238–240] (stars), as well as ZnO (REF.[241]) and WO_3 (REF.[242]) nanowires (circles) and TiO_2 (REF.[243]) and ZnS (REF.[244]) nanoparticles (triangles). The data point marked by the arrow indicates results from REF.[22]. **c** | Network conductivity plotted versus nanosheet bandgap for a wide range of nanosheet networks. **d** | Data from REF.[74] for graphene network conductivity as a function of mean nanosheet length. The lines are plots of Eq. 3 (dashed line) and Eq. 4 (solid line), combined with $t_{NS} = L_{NS}/k$ (k is the nanosheet aspect ratio), using the parameters: $n_{NS} = 10^{25}\ m^{-3}$, $P_{Net} = 0.5$, $k = 200$ and $R_J = 3{,}000\ \Omega$. **e** | Network conductivity plotted versus values of junction resistance calculated using Eqs 3 and 4 for conducting and semiconducting nanosheets, respectively, using the data in panel **a**. **f** | Ratio of junction to nanosheet resistance (R_J/R_{NS}) plotted versus junction resistance. R_J was calculated as described above. R_{NS} was estimated using $R_{NS} \approx (\sigma_{NS} t_{NS})^{-1}$ and approximating $\sigma_{NS} = 10^6\ S\ m^{-1}$ for all conducting nanosheets. For semiconductors, R_{NS} was estimated using the carrier densities quoted in REF.[224] and taking $\mu_{NS} = 50\ cm^2 V^{-1} s^{-1}$. The lines represent the boundaries between the material (M)-limited, material + junction (M+J)-limited and junction (J)-limited regimes. 2DP, 2D polymers; BP, black phosphorus.

conductivity and mobility are known from transistor studies (Supplementary Table 5 for references). These materials can be divided into two groups; the semiconductors with $n_{Net} < 10^{22}\ m^{-3}$ and the metals and semimetals with $n_{Net} > 10^{23}\ m^{-3}$. The carrier densities of the conductors are broadly in line with experimental values for the bulk precursor, such as graphite ($\sim 10^{25}\ m^{-3}$)[222] or MAX phases ($\sim 10^{27}\ m^{-3}$)[223]. However, some of the semiconductors have carrier densities below the reported bulk values for TMDs (10^{21}–$10^{23}\ m^{-3}$)[224]. Whereas part of this discrepancy is due to the presence of porosity, much of it may be due to inadvertent doping and dedoping caused by residuals from the liquid processing steps.

As illustrated by the dashed lines, which represent constant values of network mobility, these networks tend to demonstrate μ_{Net} in the relatively narrow range 0.01–10 $cm^2 V^{-1} s^{-1}$, with only graphene networks displaying higher mobilities up to ~100 $cm^2 V^{-1} s^{-1}$. These values are at least two orders of magnitude lower than the nanosheet mobilities of ~50, ~100 and >10,000 $cm^2 V^{-1} s^{-1}$ for TMDs[21], MXenes[152] and graphene[225] nanosheets, respectively. An exception to this reduced mobility is the MoS_2 data point ($\sigma_{Net} \sim 0.5\ S\ m^{-1}$) from REF.[58] (FIG. 2g), which is consistent with very a high network mobility of ~10 $cm^2 V^{-1} s^{-1}$, close to the mobility measured for the constituent nanosheets[58]. In this case, nanosheet flexibility leads to large-area junctions, resulting in a low junction resistance and, thus, shifting the rate-limiting factor to the resistance of the nanosheets themselves. By contrast, for the rigid nanosheets such as those shown in FIG. 2e, junctions tend to have limited overlap area, leading to a large junction resistance and low network mobility (~0.1 $cm^2 V^{-1} s^{-1}$). Similarly, pressed pellets of 2D polymers show high mobilities of 5 and 22 $cm^2 V^{-1} s^{-1}$ (REFS[226,227]), which may be due to their high flexibility.

Analogies with nanotube networks and nanoparticle arrays

Networks of CNTs[58] and arrays of colloidal nanocrystals[228] are electrically analogous to nanosheet networks. It is well known that nanotube networks are electrically limited by the inter-tube junctions, which display resistances that are ~10–10^4 times larger than those of the nanotubes themselves[229]. This leads to network mobilities that scale with nanotube length[203] and show thermally activated behaviour at intermediate to high temperature[168]. This behaviour is typically

Arrhenius-like ($\sigma_{Net} \propto \mu_{Net} \propto \exp(-E_a/kT)$, where E_a is an activation energy) and is usually associated with inter-tube hopping. In addition, tunnelling-like behaviour is usually observed at low temperature[229]. Interestingly, the network mobility appears to depend on the nanotube band structure[205,229], with some suggestion that the mobility activation energy is related to the bandgap[229]. Accordingly, although junctions clearly limit the electrical properties of networks, a full understanding of the network mobility requires consideration of the intrinsic nanotube properties[205], although how this should be achieved is unclear.

The study of networks of colloidal nanocrystals is also relatively mature compared with that of nanosheet networks[228]. As with nanotube networks, the mobility of arrays of colloidal nanocrystals is generally limited by inter-crystal hopping[230], leading to thermally activated behaviour that, again, is often Arrhenius-like[228,231]. However, a range of strategies have been developed to promote inter-particle charge transfer and reduce junction resistance[230–232], although junction effects alone cannot fully describe conduction, even in the weakly coupled hopping regime[230].

Work on arrays of relatively large (~20 nm) semiconducting nanocrystals[230] is relevant here, particularly to networks of relatively thick, liquid-phase-exfoliated nanosheets that may not show strong 2D characteristics. Through temperature-dependent field-effect transistor measurements, both carrier density and mobility were shown to display Arrhenius-like behaviour, each with an associated activation energy, such that the overall activation energy is: $E_a = E_{a,n} + E_{a,\mu}$, where $E_{a,n}$ describes thermal generation of mobile carriers and $E_{a,\mu}$ describes inter-particle hopping. This behaviour suggests that, in the simplest case, the network properties that are intrinsic to the material are described by the carrier density, whereas the extrinsic, junction-related properties are contained within the mobility.

This observation can be extended to WS_2/graphene nanosheet composites, where the network carrier density depends sensitively on the graphene loading, and approaches the intrinsic graphene carrier density at high graphene loading, indicating a link between the network and nanosheet carrier densities[181]. In addition, compression studies on graphene networks show network conductivity to scale with porosity roughly as $(1 - P_{Net})$[20]. Combining these observations suggests that the network carrier density can be approximated as $n_{Net} = (1 - P_{Net})n_{NS}$, where n_{Net} and n_{NS} are the network and nanosheet carrier densities, respectively. This leads to the expression:

$$\sigma_{Net} = (1 - P_{Net})n_{NS}e\mu_{Net} \quad (1)$$

Temperature dependence and activation energies

The study of the electrical properties of nanosheet networks is still relatively immature, such that the typical studies used to reveal charge transport mechanisms in disordered materials through a combination of temperature-dependent, magnetic-field-dependent and electric-field-dependent measurements[233] have not been widely performed. However, it is worth considering the mechanistic studies performed so far, which were generally limited to measuring the temperature dependence of the network conductivity.

The temperature-dependent conductivity of MXene networks is predominately described by variable-range hopping[233], with a number of materials showing the presence of an additional Arrhenius-like component at higher temperatures ($E_a = 0.015–0.1$ eV)[106]. A number of different models have been used to describe the temperature dependence of graphene networks; the most common is variable-range hopping[106,234,235], with some reports showing Arrhenius-like behaviour with relatively low activation energies of ~0.05–0.15 eV (REFS[127,236,237]). Interestingly, the temperature dependence of networks of semiconducting nanosheets appears to be solely described by Arrhenius behaviour, with activation energies between 0.05 and 0.86 eV, although there are limited data available[21,22,202]. Such behaviour is consistent with that of most nanocrystal networks[21,230] and networks of semiconducting nanotubes[168] (the latter tend to display Arrhenius-like behaviour near room temperature, with tunnelling-like behaviour dominating at low temperature).

The activation energies for semiconducting nanosheet networks are typically much larger than those for semimetal and metallic nanosheet networks. To visualize this trend, the activation energy for networks of both conducting and semiconducting nanosheets is plotted versus nanosheet bandgap in FIG. 5b (these networks all had channel lengths longer than 20 μm, most likely making them bulk-limited, such that the Schottky barriers at the contacts have minimal impact on the temperature dependence). For comparison, equivalent data for networks of 1D[168,238–242] and 0D[243,244] particles have been included. As bandgap increases, a reasonably well defined increase in E_a from ~0.1 eV for the conducting materials to ~0.85 eV for BiOCl nanosheet networks is observed[245]. This behaviour is consistent with that observed in REF.[230], assuming $E_{a,\mu}$ and/or $E_{a,n}$ increase with bandgap.

Further insight can be gained by noting that almost all the data points in FIG. 5b were extracted from temperature-dependent conductivity (or resistivity) data. The exception is an electrolytically gated WS_2 network that was measured in the on state with the ions frozen in place (marked by the arrow)[22]. The carrier density then becomes largely temperature-independent, meaning that the activation energy describes the temperature dependence of network mobility ($E_{a,\mu}$). As a result, this activation energy (50 meV) is lower than those extracted from conductivity measurements for other TMDs but similar to the mean activation energy displayed by the zero-bandgap nanosheet networks (80 meV). This value is also consistent with the mobility and hopping activation energies reported for other nanoscale semiconductors (25–100 meV in nanocrystal networks[228] and 20–100 meV in semiconducting single-wall CNT networks[168,228]).

Although the available activation energy data are sparse, this analysis is consistent with conductivity data. Because the conductivity is given by $\sigma_{Net} \propto \exp(-E_a/kT)$, the quasilinear scaling of activation energy with bandgap shown in FIG. 5b implies a near-exponential scaling of the

network conductivity with bandgap. To test this prediction, we collected published conductivity values for as many different nanosheet networks as possible and plotted σ_{Net} versus the bandgap (FIG. 5c and Supplementary Table 5). Unsurprisingly, networks fabricated from metals or semimetals such as graphene and MXenes display much higher conductivities than any of the semiconducting materials. For the semiconductors, there is a well-defined correlation between conductivity and bandgap, with conductivity increasing from ~10^{-8} S m^{-1} for a wide-bandgap material (BiOCl)[245] to 1 S m^{-1} for networks of thick phosphorene flakes[246]. This roughly exponential trend is consistent with the data in FIG. 5b. The scatter can be attributed to variations in network mobility, which may be related to differences in film morphology.

Approximate equations for network mobility and conductivity

The analysis of electronic conduction in nanosheet networks would greatly benefit from the development of a model relating network conductivity to parameters such as nanosheet carrier density and dimensions, as well as junction resistance and porosity. Until such a general equation is developed, it is worth attempting to find approximate equations, valid under certain narrow circumstances, to elucidate some general properties.

To do this, one can consider various regimes based on the relative magnitudes of R_J and R_{NS}. Clearly, the ratio R_J/R_{NS} is an important parameter and determines whether conduction is limited by junctions (J-limited), the material itself (M-limited) or a combination of both (M+J-limited). For large-area junctions such as those in REF.[58] (FIG. 2g), the junction resistance is probably low, as evidenced by the similar nanosheet and network mobilities. Such a system is probably material-limited, with $R_J \ll R_{NS}$. Under these circumstances, the network conductivity can be estimated via Eq. 1 using $\mu_{Net} \approx \mu_{NS}$:

$$\begin{aligned} \sigma_{Net,M} &\sim (1 - P_{Net}) n_{NS} e \mu_{NS} \\ \mu_{Net,M} &\sim \mu_{NS} \quad \text{(M-limited)} \end{aligned} \tag{2}$$

Alternatively, for highly conductive nanosheets, the junction resistance is expected to completely dominate (J-limited, $R_J \gg R_{NS}$). It was shown that the resistance of a network of nanoconductors is the sum of terms associated with the resistance of all the junctions[114] ($R_{Net\text{-}J}$) and the resistance of all the conductors ($R_{Net\text{-}NS}$): $R_{Net} \approx R_{Net\text{-}NS} + R_{Net\text{-}J}$. The same paper also showed that $R_{Net\text{-}NS}/R_{Net\text{-}J} \approx R_{NS}/R_J$, where R_{NS} and R_J are the resistances of an individual nanosheet and an individual junction, respectively. This is an important result, as it is easy to show (Supplementary Information) that it leads directly to an equation for the conductivity of a J-limited network and, via Eq. 1, its effective mobility:

$$\begin{aligned} \sigma_{Net,J} &\approx (1 - P_{Net}) \,/\, t_{NS} R_J \\ \mu_{Net,J} &\approx (n_{NS} e t_{NS} R_J)^{-1} \quad \text{(J-limited)} \end{aligned} \tag{3}$$

Interestingly, this equation implies that the conductivity depends on nanosheet thickness and not length, as might be expected. Although LPE-produced networks of graphene[74] and WS_2 (REF.[22]) display a conductivity that scales with length, this observation is not conclusive, as liquid-phase-exfoliated nanosheets show $L_{NS} \propto t_{NS}$ (REF.[50]). Indeed, the data in FIG. 4b (from REF.[62]) measured on electrochemically exfoliated nanosheets for which length and thickness are not known to be coupled, suggest that thickness is the relevant variable.

For many semiconducting nanosheets, R_J/R_{NS} might be neither extremely small nor extremely large, and both material and junction effects could determine network conductivity (M+J-limited), $\sigma_{Net,M\text{-}J}$. Here, both nanosheet properties and the junction resistance must be considered ($R_J \sim R_{NS}$). This is a more complicated situation, with no published solution. In the absence of an equation to describe $\sigma_{Net,M\text{-}J}$, we attempt to tentatively outline some of its likely features.

Such an equation would include R_J and, in line with Eq. 1, would probably incorporate $(1 - P_{Net})$ and n_{NS}. It would also include a parameter describing nanosheet size, which is likely to be the nanosheet thickness, t_{NS}, following Eq. 3 (although we cannot rule out the possibly that nanosheet length might be important here). In the absence of a model relating $\sigma_{Net,M\text{-}J}$ to these parameters, a possible relationship can be identified via dimensional analysis using the parameters given above. This yields an equation for $\sigma_{Net,M\text{-}J}$, which can be combined with Eq. 1 to give an effective network mobility:

$$\begin{aligned} \sigma_{Net,M+J} &\approx (1 - P_{Net}) n_{NS} t_{NS}^2 / R_J \\ \mu_{Net,M+J} &\approx t_{NS}^2 / e R_J \quad \text{(M+J-limited)} \end{aligned} \tag{4}$$

It is worth noting that Eq. 4 is consistent with the result in REF.[230] that the activation energy has two components ($E_a = E_{a,n} + E_{a,\mu}$), assuming $n_{NS} \propto \exp(-E_{a,n}/kT)$ and $R_J \propto \exp(E_{a,\mu}/kT)$.

In Eqs 2–4, the conduction regime (M, M+J or J) is clearly determined by the dependence of conductivity or mobility on nanosheet thickness, allowing the models to be tested. The data in FIG. 4b (from REF.[62]) are clearly J-limited and can be well fit by Eq. 3, yielding $R_J = 1$ MΩ (dashed line, using $n_{NS} = 1.5 \times 10^{25}$ m^{-3} as reported in the paper). This R_J value is higher than reported values of $R_J \sim 10$ kΩ for graphene networks[32,58], and the discrepancy is likely due to the low annealing temperature used.

A sample set containing a broad range of nanosheet thicknesses might cross over from one regime to another, leading to behaviour that is not consistent with any one of these equations. For example, data on σ_{Net} versus L_{NS} published in REF.[74] show an unexpected non-monotonic behaviour (FIG. 5d). This behaviour can be interpreted as a transition from M+J-limited conductivity for small nanosheets to solely J-limited conductivity for large nanosheets. The two regimes can be analysed separately using modified versions of Eqs 2–4, converting nanosheet thickness to length via the aspect ratio $k = L_{NS}/t_{NS}$ (k is roughly constant for liquid-phase-exfoliated nanosheets of a given type)[50]. Plotting Eqs 2–4 yields lines that match the data quite well and output sensible values of $k = 200$ and $R_J = 3$ kΩ (assuming $n_{NS} = 10^{25}$ m^{-3}, $P_{Net} = 0.5$). This junction resistance is reasonably close to reported values

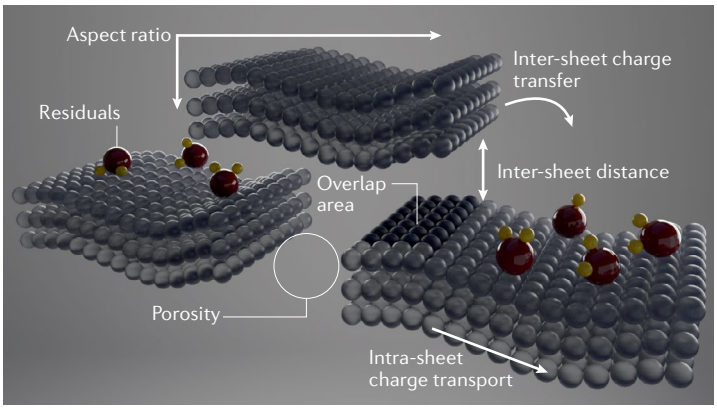

Property	Requirement for low R_J
Aspect ratio	High
Bending stiffness	Low
Bandgap	Narrow
Carrier density	High
Ink residuals	Few
Inter-sheet distance	Small
Network porosity	Low
Overlap area	Large

Fig. 6 | **Properties affecting junction resistance.** A variety of material and network properties contribute to the junction resistance, which means that a system where the junction resistance is minimized will require careful, and likely complex, optimization. Image courtesy of Katarzyna Stachura.

($R_J = \sim 10\,k\Omega$)[32,58]. This agreement between model and data provides strong evidence to support our approach.

The ideas behind Eqs 2–4 are simple and are intended to provide rough approximations for network behaviour, rather than capture the full physics of the conduction processes. There are clearly a number of limitations; for example, any complete conductivity equation should contain $R_{NS} + R_J$ (REFS[113,114]), and the uncertainty over the importance of nanosheet length or thickness requires a full theoretical analysis. Nevertheless, these equations capture the essence of these systems and can provide a basis for exploring these ideas in future work. For example, within this very simple model, all the junction properties, including nanosheet separation, interfacial area and activation energy, are effectively distilled into one parameter, the junction resistance. More work, both experimental and theoretical, will be required to shine further light on R_J. However, the discussions above would imply that $R_J \propto \mu^{-1}_{Net} \propto \exp(E_{a,\mu}/kT)$. This expression is consistent with a very recent paper that used covalent cross-linking to reduce R_J, resulting in an increase in μ_{Net}, coupled with a decrease in E_a (REF.[247]).

Junction resistance estimates

Finally, the junction resistances can be estimated for each conduction regime. Equations 3 and 4 can be applied to the data reported in FIG. 5a and Supplementary Table 5 (excluding the point from REF.[58], indicated by the arrow, which is clearly M-limited) to estimate values of R_J for networks of semiconducting and conducting nanosheets, respectively. The resultant data for R_J are plotted in FIG. 5e as a graph of σ_{Net} versus R_J. The conducting nanosheets typically have junction resistances of ~kΩ to ~MΩ, with similar geometric means of 20–25 kΩ for graphene and MXenes (to compare with reported values of R_J~10 kΩ for graphene)[32,58]. The semiconducting networks have higher values of 20–60 MΩ, comparable with values of 400 MΩ estimated for MoS_2/polymer composites[113]. The large value of R_J~20 MΩ for semiconducting, liquid-phase-exfoliated nanosheets is a major limiting factor. By contrast, thin, large-area semiconducting electrochemically exfoliated nanosheets can have R_J as low as 500 Ω (REF.[119]).

These values for the junction resistance can be combined with approximate values of nanosheet in-plane conductivity (using $R_{NS} \approx L_{NS}/\sigma_{NS}L_{NS}t_{NS} = (\sigma_{NS}t_{NS})^{-1}$) to estimate R_J/R_{NS}, as shown in FIG. 5f. The liquid-phase-exfoliated MoS_2 nanosheets with small-area junctions are largely consistent with $R_J \sim R_{NS}$. Most conductive nanosheet networks tend to display $R_J \gg R_{NS}$ as expected, although some have values of R_J comparable with R_{NS}.

Returning to FIG. 5d and considering the critical nanosheet thickness ($t_{NS} = L_{NS}/k = 5$ nm), where the lines representing the M+J-limited and J-limited regimes intersect, the crossover point between the regimes can be estimated to occur at R_J/R_{NS}~10. For symmetry reasons, the transition from M+J-limited to M-limited conduction probably occurs when R_J/R_{NS}~0.1. These boundaries have been plotted as horizontal lines in FIG. 5f. These results are consistent with the idea that conductive nanosheet networks are J-limited, whereas semiconducting nanosheet networks are mostly M+J-limited. Finally, the dependence of the junction resistance on the various material and network properties is illustrated in FIG. 6.

Conclusions and outlook

We have discussed how solution processing can yield nanosheet inks that can be printed into patterned networks in a number of ways. These networks can be constructed from conducting, semiconducting or insulating nanosheets, and can function as a variety of electronic components, such as electrodes, active layers or dielectric components, that can be combined to fabricate devices.

We have shown that electronic conduction in nanosheet networks is governed by a complex interplay between exfoliation, nanosheet dimensions, stabilization method, stabilization residuals, deposition methods and the various post-treatments. Each of these variables contributes to the network morphology, which, in turn, determines the junction resistance and, ultimately, the network mobility. We have proposed simple models relating network conductivity to junction resistance.

Improving the network mobility will be central to optimizing the electronic conduction through a nanosheet network, and the discussions in this Review suggest three primary strategies for its maximization. First, the

aspect ratio of the nanosheets should be as large as possible to create large-area, intimately contacted junctions. Second, nanosheet alignment and network porosity should be investigated and quantified so that future networks can be optimized to facilitate low-resistance junctions. Third, once junction resistance is minimized, nanosheets with a high intrinsic mobility will be needed to minimize the material contribution to the resistance and create high-performance devices.

It is clear that much needs to be done to convert nanosheet networks from an interesting research playground to a viable contender in the competitive area of printed electronics. However, we believe it is now clear that 2D materials have what it takes to make the grade for commercial realization, provided advances can be made in solution processing and network formation.

Published online: 09 November 2021

1. Akinwande, D. et al. A review on mechanics and mechanical properties of 2D materials — Graphene and beyond. *Extreme Mech. Lett.* **13**, 42–77 (2017).
2. Ferrari, A. C. et al. Science and technology roadmap for graphene, related two-dimensional crystals, and hybrid systems. *Nanoscale* **7**, 4598–4810 (2015).
3. Mounet, N. et al. Two-dimensional materials from high-throughput computational exfoliation of experimentally known compounds. *Nat. Nanotechnol.* **13**, 246–252 (2018).
4. Das, S., Chen, H.-Y., Penumatcha, A. V. & Appenzeller, J. High performance multilayer MoS_2 transistors with scandium contacts. *Nano Lett.* **13**, 100–105 (2013).
5. Zhang, Y., Ye, J., Matsuhashi, Y. & Iwasa, Y. Ambipolar MoS_2 thin flake transistors. *Nano Lett.* **12**, 1136–1140 (2012).
6. Cui, X. et al. Multi-terminal transport measurements of MoS_2 using a van der Waals heterostructure device platform. *Nat. Nanotechnol.* **10**, 534–540 (2015).
7. Cheng, R. et al. Electroluminescence and photocurrent generation from atomically sharp WSe_2/MoS_2 heterojunction *p–n* diodes. *Nano Lett.* **14**, 5590–5597 (2014).
8. Salehzadeh, O., Tran, N. H., Liu, X., Shih, I. & Mi, Z. Exciton kinetics, quantum efficiency, and efficiency droop of monolayer MoS_2 light-emitting devices. *Nano Lett.* **14**, 4125–4130 (2014).
9. Ross, J. S. et al. Electrically tunable excitonic light-emitting diodes based on monolayer WSe_2 p–n junctions. *Nat. Nanotechnol.* **9**, 268–272 (2014).
10. Cho, A.-J., Song, M.-K., Kang, D.-W. & Kwon, J.-Y. Two-dimensional WSe_2/MoS_2 p–n heterojunction-based transparent photovoltaic cell and its performance enhancement by fluoropolymer passivation. *ACS Appl. Mater. Interfaces* **10**, 35972–35977 (2018).
11. Monajjemi, M. Metal-doped graphene layers composed with boron nitride–graphene as an insulator: a nano-capacitor. *J. Mol. Model.* **20**, 2507 (2014).
12. Xu, Z. et al. Large-area growth of multi-layer hexagonal boron nitride on polished cobalt foils by plasma-assisted molecular beam epitaxy. *Sci. Rep.* **7**, 43100 (2017).
13. Zheng, Y. et al. Gate-controlled nonvolatile graphene-ferroelectric memory. *Appl. Phys. Lett.* **94**, 163505 (2009).
14. Hong, A. J. et al. Graphene flash memory. *ACS Nano* **5**, 7812–7817 (2011).
15. Coleman, J. N. et al. Two-dimensional nanosheets produced by liquid exfoliation of layered materials. *Science* **331**, 568–571 (2011).
16. Torrisi, F. et al. Inkjet-printed graphene electronics. *ACS Nano* **6**, 2992–3006 (2012).
17. Hu, G. et al. Functional inks and printing of two-dimensional materials. *Chem. Soc. Rev.* **47**, 3265–3300 (2018).
18. Garlapati, S. K. et al. Printed electronics based on inorganic semiconductors: from processes and materials to devices. *Adv. Mater.* **30**, 1707600 (2018).
19. Bonaccorso, F., Bartolotta, A., Coleman, J. N. & Backes, C. 2D-crystal-based functional inks. *Adv. Mater.* **28**, 6136–6166 (2016).
20. Barwich, S. et al. On the relationship between morphology and conductivity in nanosheet networks. *Carbon* **171**, 306–319 (2021).
21. Kelly, A. G. et al. All-printed thin-film transistors from networks of liquid-exfoliated nanosheets. *Science* **356**, 69–72 (2017).
22. Higgins, T. M. et al. Electrolyte-gated n-type transistors produced from aqueous inks of WS_2 nanosheets. *Adv. Funct. Mater.* **29**, 1804387 (2018).
23. Finn, D. J. et al. Inkjet deposition of liquid-exfoliated graphene and MoS_2 nanosheets for printed device applications. *J. Mater. Chem. C* **2**, 925–932 (2014).
24. Ghosh, S. et al. Ultrafast intrinsic photoresponse and direct evidence of sub-gap states in liquid phase exfoliated MoS_2 thin films. *Sci. Rep.* **5**, 1172 (2015).
25. Kelly, A. G., Finn, D., Harvey, A., Hallam, T. & Coleman, J. N. All-printed capacitors from graphene-BN-graphene nanosheet heterostructures. *Appl. Phys. Lett.* **109**, 023107 (2016).
26. Worsley, R. et al. All-2D material inkjet-printed capacitors: toward fully printed integrated circuits. *ACS Nano* **13**, 54–60 (2018).
27. Carey, T. et al. Fully inkjet-printed two-dimensional material field-effect heterojunctions for wearable and textile electronics. *Nat. Commun.* **8**, 1202 (2017).
28. Zhang, C. et al. Additive-free MXene inks and direct printing of micro-supercapacitors. *Nat. Commun.* **10**, 1795 (2019).
29. Parvez, K. et al. Exfoliation of graphite into graphene in aqueous solutions of inorganic salts. *J. Am. Chem. Soc.* **136**, 6083–6091 (2014).
30. Guyot-Sionnest, P. Electrical transport in colloidal quantum dot films. *J. Phys. Chem. Lett.* **3**, 1169–1175 (2012).
31. Nirmalraj, P. N., Lyons, P. E., De, S., Coleman, J. N. & Boland, J. J. Electrical connectivity in single-walled carbon nanotube networks. *Nano Lett.* **9**, 3890–3895 (2009).
32. Nirmalraj, P. N., Lutz, T., Kumar, S., Duesberg, G. S. & Boland, J. J. Nanoscale mapping of electrical resistivity and connectivity in graphene strips and networks. *Nano Lett.* **11**, 16–22 (2011).
33. Cunningham, G., Hanlon, D., McEvoy, N., Duesberg, G. S. & Coleman, J. N. Large variations in both dark- and photoconductivity in nanosheet networks as nanomaterial is varied from MoS_2 to WTe_2. *Nanoscale* **7**, 198–208 (2014).
34. Huang, Q. & Zhu, Y. Printing conductive nanomaterials for flexible and stretchable electronics: a review of materials, processes, and applications. *Adv. Mater. Technol.* **4**, 1800546 (2019).
35. Ng, L. W. T. et al. *Printing of Graphene and Related 2D Materials* (Springer, 2019).
36. Torrisi, F. & Carey, T. Graphene, related two-dimensional crystals and hybrid systems for printed and wearable electronics. *Nano Today* **23**, 73–96 (2018).
37. Witomska, S., Leydecker, T., Ciesielski, A. & Samorì, P. Production and patterning of liquid phase–exfoliated 2D sheets for applications in optoelectronics. *Adv. Funct. Mater.* **29**, 1901126 (2019).
38. Paton, K. R. et al. Scalable production of large quantities of defect-free few-layer graphene by shear exfoliation in liquids. *Nat. Mater.* **13**, 624–630 (2014).
39. Varrla, E. et al. Large-scale production of size-controlled MoS_2 nanosheets by shear exfoliation. *Chem. Mater.* **27**, 1129–1139 (2015).
40. Secor, E. B. et al. Enhanced conductivity, adhesion, and environmental stability of printed graphene inks with nitrocellulose. *Chem. Mater.* **29**, 2332–2340 (2017).
41. Biccai, S. et al. Exfoliation of 2D materials by high shear mixing. *2D Mater.* **6**, 015008 (2018).
42. Del Rio Castillo, A. E. et al. High-yield production of 2D crystals by wet-jet milling. *Mater. Horiz.* **5**, 890–904 (2018).
43. Bellani, S. et al. Scalable production of graphene inks via wet-jet milling exfoliation for screen-printed micro-supercapacitors. *Adv. Funct. Mater.* **29**, 1807659 (2019).
44. Paton, K. R., Anderson, J., Pollard, A. J. & Sainsbury, T. Production of few-layer graphene by microfluidization. *Mater. Res. Express* **4**, 025604 (2017).
45. Karagiannidis, P. G. et al. Microfluidization of graphite and formulation of graphene-based conductive inks. *ACS Nano* **11**, 2742–2755 (2017).
46. Xu, Y., Cao, H., Xue, Y., Li, B. & Cai, W. Liquid-phase exfoliation of graphene: an overview on exfoliation media, techniques, and challenges. *Nanomaterials* **8**, 942 (2018).
47. Hernandez, Y. et al. High-yield production of graphene by liquid-phase exfoliation of graphite. *Nat. Nanotechnol.* **3**, 563–568 (2008).
48. Lotya, M. et al. Liquid phase production of graphene by exfoliation of graphite in surfactant/water solutions. *J. Am. Chem. Soc.* **131**, 3611–3620 (2009).
49. May, P., Khan, U., Hughes, J. M. & Coleman, J. N. Correction to "Role of solubility parameters in understanding the steric stabilization of exfoliated two-dimensional nanosheets by adsorbed polymers". *J. Phys. Chem. C* **116**, 24390–24391 (2012).
50. Backes, C. et al. Equipartition of energy defines the size–thickness relationship in liquid-exfoliated nanosheets. *ACS Nano* **13**, 7050–7061 (2019).
51. Li, Z. et al. Mechanisms of liquid-phase exfoliation for the production of graphene. *ACS Nano* **14**, 10976–10985 (2020).
52. Backes, C. et al. Production of highly monolayer enriched dispersions of liquid-exfoliated nanosheets by liquid cascade centrifugation. *ACS Nano* **10**, 1589–1601 (2016).
53. Ott, S. et al. Impact of the MoS_2 starting material on the dispersion quality and quantity after liquid phase exfoliation. *Chem. Mater.* **31**, 8424–8431 (2019).
54. García-Dalí, S. et al. Aqueous cathodic exfoliation strategy toward solution-processable and phase-preserved MoS_2 nanosheets for energy storage and catalytic applications. *ACS Appl. Mater. Interfaces* **11**, 36991–37003 (2019).
55. Cooper, A. J., Wilson, N. R., Kinloch, I. A. & Dryfe, R. A. W. Single stage electrochemical exfoliation method for the production of few-layer graphene via intercalation of tetraalkylammonium cations. *Carbon* **66**, 340–350 (2014).
56. El Garah, M. et al. MoS_2 nanosheets via electrochemical lithium-ion intercalation under ambient conditions. *FlatChem* **9**, 33–39 (2018).
57. Zeng, Z. et al. Single-layer semiconducting nanosheets: high-yield preparation and device fabrication. *Angew. Chem.* **123**, 11289–11293 (2011).
58. Lin, Z. et al. Solution-processable 2D semiconductors for high-performance large-area electronics. *Nature* **562**, 254–258 (2018).
59. Xu, Y. Z. et al. Monolayer MoS_2 with S vacancies from interlayer spacing expanded counterparts for highly efficient electrochemical hydrogen production. *J. Mater. Chem. A* **4**, 16524–16530 (2016).
60. Li, F. et al. Advanced composite 2D energy materials by simultaneous anodic and cathodic exfoliation. *Adv. Energy Mater.* **8**, 1702794 (2018).
61. Parvez, K., Worsley, R., Alieva, A., Felten, A. & Casiraghi, C. Water-based and inkjet printable inks made by electrochemically exfoliated graphene. *Carbon* **149**, 213–221 (2019).
62. Yakimchuk, E., Soots, R., Kotin, I. & Antonova, I. 2D printed graphene conductive layers with high carrier mobility. *Curr. Appl. Phys.* **17**, 1655–1661 (2017).
63. Capasso, A. et al. Ink-jet printing of graphene for flexible electronics: an environmentally-friendly approach. *Solid State Commun.* **224**, 53–63 (2015).
64. Kelly, A. G., Vega-Mayoral, V., Boland, J. B. & Coleman, J. N. Whiskey-phase exfoliation: exfoliation and printing of nanosheets using Irish whiskey. *2D Mater.* **6**, 045036 (2019).
65. Arapov, K. et al. Conductive screen printing inks by gelation of graphene dispersions. *Adv. Funct. Mater.* **26**, 586–593 (2016).
66. Hyun, W. J., Secor, E. B., Hersam, M. C., Frisbie, C. D. & Francis, L. F. High-resolution patterning of graphene by screen printing with a silicon stencil for highly flexible printed electronics. *Adv. Mater.* **27**, 109–115 (2015).

67. Xu, Y. et al. Screen-printable thin film supercapacitor device utilizing graphene/polyaniline inks. *Adv. Energy Mater.* **3**, 1035–1040 (2013).
68. Juntunen, T. et al. Inkjet printed large-area flexible few-layer graphene thermoelectrics. *Adv. Funct. Mater.* **28**, 1800480 (2018).
69. Secor, E. B., Prabhumirashi, P. L., Puntambekar, K., Geier, M. L. & Hersam, M. C. Inkjet printing of high conductivity, flexible graphene patterns. *J. Phys. Chem. Lett.* **4**, 1347–1351 (2013).
70. Li, J. et al. Efficient inkjet printing of graphene. *Adv. Mater.* **25**, 3985–3992 (2013).
71. McManus, D. et al. Water-based and biocompatible 2D crystal inks for all-inkjet-printed heterostructures. *Nat. Nanotechnol.* **12**, 343–350 (2017).
72. Majee, S., Liu, C., Wu, B., Zhang, S. L. & Zhang, Z. B. Ink-jet printed highly conductive pristine graphene patterns achieved with water-based ink and aqueous doping processing. *Carbon* **114**, 77–83 (2017).
73. Ding, H. et al. Water-based highly conductive graphene inks for fully printed humidity sensors. *J. Phys. D* **53**, 455304 (2020).
74. Large, M. J. et al. Large-scale surfactant exfoliation of graphene and conductivity-optimized graphite enabling wireless connectivity. *Adv. Mater. Technol.* **5**, 000284 (2020).
75. Carey, T., Jones, C., Le Moal, F., Deganello, D. & Torrisi, F. Spray-coating thin films on three-dimensional surfaces for a semitransparent capacitive-touch device. *ACS Appl. Mater. Interfaces* **10**, 19948–19956 (2018).
76. Barwich, S., Coleman, J. N. & Möbius, M. E. Yielding and flow of highly concentrated, few-layer graphene suspensions. *Soft Matter* **11**, 3159–3164 (2015).
77. He, P. et al. Screen-printing of a highly conductive graphene ink for flexible printed electronics. *ACS Appl. Mater. Interfaces* **11**, 32225–32234 (2019).
78. Leng, T. et al. Screen-printed graphite nanoplate conductive ink for machine learning enabled wireless radiofrequency-identification sensors. *ACS Appl. Nano Mater.* **2**, 6197–6208 (2019).
79. Pan, K. et al. Sustainable production of highly conductive multilayer graphene ink for wireless connectivity and IoT applications. *Nat. Commun.* **9**, 5197 (2018).
80. Lynch, P. J. et al. Graphene-based printable conductors for cyclable strain sensors on elastomeric substrates. *Carbon* **169**, 25–31 (2020).
81. Zhang, J. et al. Scalable manufacturing of free-standing, strong $Ti_3C_2T_x$ MXene films with outstanding conductivity. *Adv. Mater.* **32**, 2001093 (2020).
82. Akbari, M. et al. Fabrication and characterization of graphene antenna for low-cost and environmentally friendly RFID tags. *IEEE Antennas Wirel. Propag. Lett.* **15**, 1569–1572 (2016).
83. Chang, Q., Li, L., Sai, L., Shi, W. & Huang, L. Water-soluble hybrid graphene ink for gravure-printed planar supercapacitors. *Adv. Electron. Mater.* **4**, 1800059 (2018).
84. Suganuma, K. in *Introduction to Printed Electronics* 23–48 (Springer, 2014).
85. Huang, X. et al. Binder-free highly conductive graphene laminate for low cost printed radio frequency applications. *Appl. Phys. Lett.* **106**, 203105 (2015).
86. O'Suilleabhain, D. et al. Effect of the gate volume on the performance of printed nanosheet network-based transistors. *ACS Appl. Electron. Mater.* **2**, 2164–2170 (2020).
87. Li, J., Lemme, M. C. & Östling, M. Inkjet printing of 2D layered materials. *ChemPhysChem* **15**, 3427–3434 (2014).
88. Lu, S. et al. Flexible, print-in-place 1D–2D thin-film transistors using aerosol jet printing. *ACS Nano* **13**, 11263–11272 (2019).
89. van Osch, T. H. J., Perelaer, J., de Laat, A. W. M. & Schubert, U. S. Inkjet printing of narrow conductive tracks on untreated polymeric substrates. *Adv. Mater.* **20**, 343–345 (2008).
90. Tekin, E., Smith, P. J. & Schubert, U. S. Inkjet printing as a deposition and patterning tool for polymers and inorganic particles. *Soft Matter* **4**, 703–713 (2008).
91. Calvert, P. Inkjet printing for materials and devices. *Chem. Mater.* **13**, 3299–3305 (2001).
92. Sirringhaus, H. & Shimoda, T. Inkjet printing of functional materials. *MRS Bull.* **28**, 802–806 (2011).
93. Del Rio Castillo, A. E. et al. Exfoliation of few-layer black phosphorus in low-boiling-point solvents and its application in Li-ion batteries. *Chem. Mater.* **30**, 506–516 (2018).
94. Khan, U., May, P., O'Neill, A. & Coleman, J. N. Development of stiff, strong, yet tough composites by the addition of solvent exfoliated graphene to polyurethane. *Carbon* **48**, 4035–4041 (2010).
95. O'Neill, A., Khan, U. & Coleman, J. N. Preparation of high concentration dispersions of exfoliated MoS_2 with increased flake size. *Chem. Mater.* **24**, 2414–2421 (2012).
96. Eredia, M. et al. Morphology and electronic properties of electrochemically exfoliated graphene. *J. Phys. Chem. Lett.* **8**, 3347–3355 (2017).
97. Zheng, J. et al. High quality graphene with large flakes exfoliated by oleyl amine. *Chem. Commun.* **46**, 5728–5730 (2010).
98. Xia, X. et al. Aligning graphene sheets in PDMS for improving output performance of triboelectric nanogenerator. *Carbon* **111**, 569–576 (2017).
99. Cunningham, G. et al. Photoconductivity of solution-processed MoS_2 films. *J. Mater. Chem. C* **1**, 6899–6904 (2013).
100. Osada, M. et al. High-κ dielectric nanofilms fabricated from titania nanosheets. *Adv. Mater.* **18**, 1023–1027 (2006).
101. Neilson, J., Avery, M. & Derby, B. Tiled monolayer films of 2D molybdenum disulfide nanoflakes assembled at liquid/liquid interfaces. *ACS Appl. Mater. Interfaces* **12**, 25125–25134 (2020).
102. Mikolajek, M., Friedrich, A., Bauer, W. & Binder, J. R. Requirements to ceramic suspensions for inkjet printing. *Ceram. Forum Int.* **92**, 25–29 (2015).
103. de Gans, B.-J. & Schubert, U. S. Inkjet printing of well-defined polymer dots and arrays. *Langmuir* **20**, 7789–7793 (2004).
104. Pack, M., Hu, H., Kim, D.-O., Yang, X. & Sun, Y. Colloidal drop deposition on porous substrates: competition among particle motion, evaporation, and infiltration. *Langmuir* **31**, 7953–7961 (2015).
105. Calabrese, G. et al. Inkjet-printed graphene Hall mobility measurements and low-frequency noise characterization. *Nanoscale* **12**, 6708–6716 (2020).
106. Halim, J. et al. Variable range hopping and thermally activated transport in molybdenum-based MXenes. *Phys. Rev. B* **98**, 104202 (2018).
107. Richter, N. et al. Charge transport mechanism in networks of armchair graphene nanoribbons. *Sci. Rep.* **10**, 1988 (2020).
108. Bellew, A. T., Manning, H. G., da Rocha, C. G., Ferreira, M. S. & Boland, J. J. Resistance of single Ag nanowire junctions and their role in the conductivity of nanowire networks. *ACS Nano* **9**, 11422–11429 (2015).
109. da Rocha, C. G. et al. Ultimate conductivity performance in metallic nanowire networks. *Nanoscale* **7**, 13011–13016 (2015).
110. Mutiso, R. M., Sherrott, M. C., Rathmell, A. R., Wiley, B. J. & Winey, K. I. Integrating simulations and experiments to predict sheet resistance and optical transmittance in nanowire films for transparent conductors. *ACS Nano* **7**, 7654–7663 (2013).
111. Yao, H. M., Hsieh, Y. P., Kong, J. & Hofmann, M. Modelling electrical conduction in nanostructure assemblies through complex networks. *Nat. Mater.* **19**, 745–751 (2020).
112. Znidarsic, A. et al. Spatially resolved transport properties of pristine and doped single-walled carbon nanotube networks. *J. Phys. Chem. C* **117**, 13324–13330 (2013).
113. Biccai, S. et al. Negative gauge factor piezoresistive composites based on polymers filled with MoS_2 nanosheets. *ACS Nano* **13**, 6845–6855 (2019).
114. Ponzoni, A. The contributions of junctions and nanowires/nanotubes in conductive networks. *Appl. Phys. Lett.* **114**, 153105 (2019).
115. Stern, A. et al. Conductivity enhancement of transparent 2D carbon nanotube networks occurs by resistance reduction in all junctions. *J. Phys. Chem. C* **122**, 14872–14876 (2018).
116. Hauquier, F. et al. Conductive-probe AFM characterization of graphene sheets bonded to gold surfaces. *Appl. Surf. Sci.* **258**, 2920–2926 (2012).
117. Hu, L. B., Kim, H. S., Lee, J. Y., Peumans, P. & Cui, Y. Scalable coating and properties of transparent, flexible, silver nanowire electrodes. *ACS Nano* **4**, 2955–2963 (2010).
118. Selzer, F. et al. Electrical limit of silver nanowire electrodes: direct measurement of the nanowire junction resistance. *Appl. Phys. Lett.* **108**, 163302 (2016).
119. Li, J. et al. Printable two-dimensional superconducting monolayers. *Nat. Mater.* **20**, 181–187 (2020).
120. Shanmugam, M., Bansal, T., Durcan, C. A. & Yu, B. Molybdenum disulphide/titanium dioxide nanocomposite-poly 3-hexylthiophene bulk heterojunction solar cell. *Appl. Phys. Lett.* **100**, 153901 (2012).
121. Sneha, V. R. et al. Interlayer coupling and diode characteristics of heterostructures of solution processed MoS_2:ReS_2 nanocrystals. *Appl. Surf. Sci.* **505**, 144475 (2020).
122. Wang, D. et al. Hierarchical nanostructured core–shell Sn@C nanoparticles embedded in graphene nanosheets: spectroscopic view and their application in lithium ion batteries. *Phys. Chem. Chem. Phys.* **15**, 3535 (2013).
123. Hossain, R. F., Deaguero, I. G., Boland, T. & Kaul, A. B. Biocompatible, large-format, inkjet printed heterostructure MoS_2-graphene photodetectors on conformable substrates. *npj 2D Mater. Appl.* **1**, 28 (2017).
124. Wróblewski, G. & Janczak, D. Screen printed, transparent, and flexible electrodes based on graphene nanoplatelet pastes. *Proc. SPIE* **8454**, 84541E (2012).
125. Manjakkal, L., Núñez, C. G., Dang, W. & Dahiya, R. Flexible self-charging supercapacitor based on graphene-Ag-3D graphene foam electrodes. *Nano Energy* **51**, 604–612 (2018).
126. De, S. & Coleman, J. N. Are there fundamental limitations on the sheet resistance and transmittance of thin graphene films? *ACS Nano* **4**, 2713–2720 (2010).
127. Kong, D., Le, L. T., Li, Y., Zunino, J. L. & Lee, W. Temperature-dependent electrical properties of graphene inkjet-printed on flexible materials. *Langmuir* **28**, 13467–13472 (2012).
128. Arapov, K. et al. Graphene screen-printed radio-frequency identification devices on flexible substrates. *Phys. Status Solidi RRL* **10**, 812–818 (2016).
129. Shen, B., Zhai, W. & Zheng, W. Ultrathin flexible graphene film: an excellent thermal conducting material with efficient EMI shielding. *Adv. Funct. Mater.* **24**, 4542–4548 (2014).
130. Sankaran, S., Deshmukh, K., Ahamed, M. B. & Khadheer Pasha, S. K. Recent advances in electromagnetic interference shielding properties of metal and carbon filler reinforced flexible polymer composites: a review. *Compos. Part A Appl. Sci. Manuf.* **114**, 49–71 (2018).
131. Li, G., Mo, X., Law, W.-C. & Chan, K. C. 3D printed graphene/nickel electrodes for high areal capacitance electrochemical storage. *J. Mater. Chem. A* **7**, 4055–4062 (2019).
132. Ervin, M. H., Le, L. T. & Lee, W. Y. Inkjet-printed flexible graphene-based supercapacitor. *Electrochim. Acta* **147**, 610–616 (2014).
133. Santra, S. et al. CMOS integration of inkjet-printed graphene for humidity sensing. *Sci. Rep.* **5**, 17374 (2015).
134. Xu, K. et al. Nanomaterial-based gas sensors: a review. *Instrum. Sci. Technol.* **46**, 115–145 (2017).
135. Yun, J. et al. Stretchable patterned graphene gas sensor driven by integrated micro-supercapacitor array. *Nano Energy* **19**, 401–414 (2016).
136. Seekaew, Y. & Wongchoosuk, C. A novel graphene-based electroluminescent gas sensor for carbon dioxide detection. *Appl. Surf. Sci.* **479**, 525–531 (2019).
137. Teengam, P. et al. Electrochemical paper-based peptide nucleic acid biosensor for detecting human papillomavirus. *Anal. Chim. Acta* **952**, 32–40 (2017).
138. Nikoleli, G.-P. et al. Structural characterization of graphene nanosheets for miniaturization of potentiometric urea lipid film based biosensors. *Electroanalysis* **24**, 1285–1295 (2012).
139. Feng, J. et al. Metallic few-layered VS_2 ultrathin nanosheets: high two-dimensional conductivity for in-plane supercapacitors. *J. Am. Chem. Soc.* **133**, 17832–17838 (2011).
140. Yang, C. et al. Metallic graphene-like VSe_2 ultrathin nanosheets: superior potassium-ion storage and their working mechanism. *Adv. Mater.* **30**, 1800036 (2018).
141. Liang, H. et al. Solution growth of vertical VS_2 nanoplate arrays for electrocatalytic hydrogen evolution. *Chem. Mater.* **28**, 5587–5591 (2016).
142. Ming, F., Liang, H., Lei, Y., Zhang, W. & Alshareef, H. N. Solution synthesis of VSe_2 nanosheets and their alkali metal ion storage performance. *Nano Energy* **53**, 11–16 (2018).
143. Ji, Q. et al. Metallic vanadium disulfide nanosheets as a platform material for multifunctional electrode applications. *Nano Lett.* **17**, 4908–4916 (2017).

144. Voiry, D. et al. Enhanced catalytic activity in strained chemically exfoliated WS_2 nanosheets for hydrogen evolution. *Nat. Mater.* **12**, 850–855 (2013).
145. Lukowski, M. A. et al. Enhanced hydrogen evolution catalysis from chemically exfoliated metallic MoS_2 nanosheets. *J. Am. Chem. Soc.* **135**, 10274–10277 (2013).
146. Lukowski, M. A. et al. Highly active hydrogen evolution catalysis from metallic WS_2 nanosheets. *Energy Environ. Sci.* **7**, 2608–2613 (2014).
147. Anasori, B., Lukatskaya, M. R. & Gogotsi, Y. 2D metal carbides and nitrides (MXenes) for energy storage. *Nat. Rev. Mater.* **2**, 16098 (2017).
148. Anasori, B. & Gogotsi, Y. (eds) *2D Metal Carbides and Nitrides (MXenes): Structure, Properties and Applications* (Springer, 2019).
149. Vural, M. et al. Inkjet printing of self-assembled 2D titanium carbide and protein electrodes for stimuli-responsive electromagnetic shielding. *Adv. Funct. Mater.* **28**, 1801972 (2018).
150. Mariano, M. et al. Solution-processed titanium carbide MXene films examined as highly transparent conductors. *Nanoscale* **8**, 16371–16378 (2016).
151. Han, M. et al. Ti_3C_2 MXenes with modified surface for high-performance electromagnetic absorption and shielding in the X-band. *ACS Appl. Mater. Interfaces* **8**, 21011–21019 (2016).
152. Li, G. et al. Dynamical control over terahertz electromagnetic interference shielding with 2D $Ti_3C_2T_y$ MXene by ultrafast optical pulses. *Nano Lett.* **20**, 636–643 (2019).
153. Li, X. et al. 2D carbide MXene Ti_2CT_x as a novel high-performance electromagnetic interference shielding material. *Carbon* **146**, 210–217 (2019).
154. Shahzad, F. et al. Electromagnetic interference shielding with 2D transition metal carbides (MXenes). *Science* **353**, 1137–1140 (2016).
155. Simon, R. M. EMI shielding through conductive plastics. *Polym. Plast. Technol. Eng.* **17**, 1–10 (2006).
156. Liu, J. et al. Hydrophobic, flexible, and lightweight MXene foams for high-performance electromagnetic-interference shielding. *Adv. Mater.* **29**, 1702367 (2017).
157. Zhou, Z. et al. Ultrathin MXene/calcium alginate aerogel film for high-performance electromagnetic interference shielding. *Adv. Mater. Interfaces* **6**, 1802040 (2019).
158. Iqbal, A. et al. Anomalous absorption of electromagnetic waves by 2D transition metal carbonitride Ti_3CNT_x (MXene). *Science* **369**, 446–450 (2020).
159. Zhu, J. et al. Layer-by-layer assembled 2D montmorillonite dielectrics for solution-processed electronics. *Adv. Mater.* **28**, 63–68 (2016).
160. Nalawade, Y. et al. All-printed dielectric capacitors from high-permittivity, liquid-exfoliated BiOCl nanosheets. *ACS Appl. Electron. Mater.* **2**, 3233–3241 (2020).
161. Moraes, A. C. M. et al. Ion-conductive, viscosity-tunable hexagonal boron nitride nanosheet inks. *Adv. Funct. Mater.* **29**, 1902245 (2019).
162. Withers, F. et al. Heterostructures produced from nanosheet-based inks. *Nano Lett.* **14**, 3987–3992 (2014).
163. Ding, Z., Xing, R., Fu, Q., Ma, D. & Han, Y. Patterning of pinhole free small molecular organic light-emitting films by ink-jet printing. *Org. Electron.* **12**, 703–709 (2011).
164. Joseph, A. M., Nagendra, B., Bhoje Gowd, E. & Surendran, K. P. Screen-printable electronic ink of ultrathin boron nitride nanosheets. *ACS Omega* **1**, 1220–1228 (2016).
165. Zhu, X. et al. Hexagonal boron nitride–enhanced optically transparent polymer dielectric inks for printable electronics. *Adv. Funct. Mater.* **30**, 2002339 (2020).
166. Gupta, B. & Matte, H. S. S. R. Solution-processed layered hexagonal boron nitride dielectrics: a route toward fabrication of high performance flexible devices. *ACS Appl. Electron. Mater.* **1**, 2130–2139 (2019).
167. Hu, H. & Larson, R. G. Marangoni effect reverses coffee-ring depositions. *J. Phys. Chem. B* **110**, 7090–7094 (2006).
168. Brohmann, M. et al. Temperature-dependent charge transport in polymer-sorted semiconducting carbon nanotube networks with different diameter distributions. *J. Phys. Chem. C* **122**, 19886–19896 (2018).
169. Castellanos-Gomez, A. et al. Isolation and characterization of few-layer black phosphorus. *2D Mater.* **1**, 025001 (2014).
170. Hanlon, D. et al. Production of molybdenum trioxide nanosheets by liquid exfoliation and their application in high-performance supercapacitors. *Chem. Mater.* **26**, 1751–1763 (2014).
171. Synnatschke, K. et al. Length- and thickness-dependent optical response of liquid-exfoliated transition metal dichalcogenides. *Chem. Mater.* **31**, 10049–10062 (2019).
172. Li, J., Naiini, M. M., Vaziri, S., Lemme, M. C. & Östling, M. Inkjet printing of MoS_2. *Adv. Funct. Mater.* **24**, 6524–6531 (2014).
173. Lee, S. K., Chu, D., Song, D. Y., Pak, S. W. & Kim, E. K. Electrical and photovoltaic properties of residue-free MoS_2 thin films by liquid exfoliation method. *Nanotechnology* **28**, 195703 (2017).
174. Lee, S. K., Chu, D., Yoo, J. & Kim, E. K. Formation of transition metal dichalcogenides thin films with liquid phase exfoliation technique and photovoltaic applications. *Sol. Energy Mater. Sol. Cell* **184**, 9–14 (2018).
175. Pataniya, P. M. et al. Photovoltaic activity of WSe_2/Si hetero junction. *Mater. Res. Bull.* **120**, 110602 (2019).
176. Adilbekova, B. et al. Liquid phase exfoliation of MoS_2 and WS_2 in aqueous ammonia and their application in highly efficient organic solar cells. *J. Mater. Chem. C* **8**, 5259–5264 (2020).
177. Tulsani, S. R., Rath, A. K. & Late, D. J. 2D-MoS_2 nanosheets as effective hole transport materials for colloidal PbS quantum dot solar cells. *Nanoscale Adv.* **1**, 1387–1394 (2019).
178. Feng, X. et al. A fully printed flexible MoS_2 memristive artificial synapse with femtojoule switching energy. *Adv. Electron. Mater.* **5**, 1900740 (2019).
179. Zaumseil, J. Single-walled carbon nanotube networks for flexible and printed electronics. *Semicond. Sci. Technol.* **30**, 074001 (2015).
180. Braga, D. & Horowitz, G. High-performance organic field-effect transistors. *Adv. Mater.* **21**, 1473–1486 (2009).
181. O'Suilleabhain, D., Vega-Mayoral, V., Kelly, A. G., Harvey, A. & Coleman, J. N. Percolation effects in electrolytically gated WS_2/graphene nano:nano composites. *ACS Appl. Mater. Interfaces* **11**, 8545–8555 (2019).
182. Zeng, X., Hirwa, H., Metel, S., Nicolosi, V. & Wagner, V. Solution processed thin film transistor from liquid phase exfoliated MoS_2 flakes. *Solid State Electron.* **141**, 58–64 (2018).
183. van Hecke, M. Jamming of soft particles: geometry, mechanics, scaling and isostaticity. *J. Phys. Condens. Matter* **22**, 033101 (2010).
184. Gao, X. et al. High-mobility patternable MoS_2 percolating nanofilms. *Nano Res.* **14**, 2255–2263 (2021).
185. Arapov, K. et al. Conductivity enhancement of binder-based graphene inks by photonic annealing and subsequent compression rolling. *Adv. Eng. Mater.* **18**, 1234–1239 (2016).
186. Jabari, E. & Toyserkani, E. Micro-scale aerosol-jet printing of graphene interconnects. *Carbon* **91**, 321–329 (2015).
187. Pandhi, T. et al. Electrical transport and power dissipation in aerosol-jet-printed graphene interconnects. *Sci. Rep.* **8**, 10842 (2018).
188. Secor, E. B. et al. Gravure printing of graphene for large-area flexible electronics. *Adv. Mater.* **26**, 4533–4538 (2014).
189. Zhang, Q. et al. Gravure-printed interdigital microsupercapacitors on a flexible polyimide substrate using crumpled graphene ink. *Nanotechnology* **27**, 105401 (2016).
190. Marchand, D. et al. Surface structure and electrical conductivity of natural and artificial graphites. *Carbon* **22**, 497–506 (1984).
191. Arapov, K., Abbel, R., de With, G. & Friedrich, H. Inkjet printing of graphene. *Faraday Discuss.* **173**, 323–336 (2014).
192. Arkhireyeva, A. & Hashemi, S. Effect of temperature on fracture properties of an amorphous poly(ethylene terephthalate) (PET) film. *J. Mater. Sci.* **37**, 3675–3683 (2002).
193. Luo, P. et al. Doping engineering and functionalization of two-dimensional metal chalcogenides. *Nanoscale Horiz.* **4**, 26–51 (2019).
194. Yamamoto, M., Einstein, T. L., Fuhrer, M. S. & Cullen, W. G. Anisotropic etching of atomically thin MoS_2. *J. Phys. Chem. C* **117**, 25643–25649 (2013).
195. Wu, J. et al. Layer thinning and etching of mechanically exfoliated MoS_2 nanosheets by thermal annealing in air. *Small* **9**, 3314–3319 (2013).
196. Potts, S.-J., Lau, Y. C., Dunlop, T., Claypole, T. & Phillips, C. Effect of photonic flash annealing with subsequent compression rolling on the topography, microstructure and electrical performance of carbon-based inks. *J. Mater. Sci.* **54**, 8163–8176 (2019).
197. Secor, E. B., Ahn, B. Y., Gao, T. Z., Lewis, J. A. & Hersam, M. C. Rapid and versatile photonic annealing of graphene inks for flexible printed electronics. *Adv. Mater.* **27**, 6683–6688 (2015).
198. Secor, E. B. et al. Combustion-assisted photonic annealing of printable graphene inks via exothermic binders. *ACS Appl. Mater. Interfaces* **9**, 29418–29423 (2017).
199. Zhai, P.-Y. et al. Calendering of free-standing electrode for lithium-sulfur batteries with high volumetric energy density. *Carbon* **111**, 493–501 (2017).
200. Huang, X. et al. Highly flexible and conductive printed graphene for wireless wearable communications applications. *Sci. Rep.* **5**, 18298 (2016).
201. Lin, X. et al. Fabrication of highly-aligned, conductive, and strong graphene papers using ultralarge graphene oxide sheets. *ACS Nano* **6**, 10708–10719 (2012).
202. Eda, G. & Chhowalla, M. Graphene-based composite thin films for electronics. *Nano Lett.* **9**, 814–818 (2009).
203. Kuwahara, Y., Nihey, F., Ohmori, S. & Saito, T. Length dependent performance of single-wall carbon nanotube thin film transistors. *Carbon* **91**, 370–377 (2015).
204. Zhu, J. et al. Thickness-dependent bandgap tunable molybdenum disulfide films for optoelectronics. *RSC Adv.* **6**, 110604–110609 (2016).
205. Brohmann, M. et al. Charge transport in mixed semiconducting carbon nanotube networks with tailored mixing ratios. *ACS Nano* **13**, 7323–7332 (2019).
206. Wood, A. J. Witten's lectures on crumpling. *Physica A* **313**, 83–109 (2002).
207. Lu, Q., Arroyo, M. & Huang, R. Elastic bending modulus of monolayer graphene. *J. Phys. D* **42**, 102002 (2009).
208. Koenig, S. P., Boddeti, N. G., Dunn, M. L. & Bunch, J. S. Ultrastrong adhesion of graphene membranes. *Nat. Nanotechnol.* **6**, 543–546 (2011).
209. Lai, K., Zhang, W.-B., Zhou, F., Zeng, F. & Tang, B.-Y. Bending rigidity of transition metal dichalcogenide monolayers from first-principles. *J. Phys. D* **49**, 185301 (2016).
210. Lin, Z. et al. Solution processable colloidal nanoplates as building blocks for high-performance electronic thin films on flexible substrates. *Nano Lett.* **14**, 6547–6553 (2014).
211. Han, E. et al. Ultrasoft slip-mediated bending in few-layer graphene. *Nat. Mater.* **19**, 305–309 (2020).
212. Huang, Y., Wu, J. & Hwang, K. C. Thickness of graphene and single-wall carbon nanotubes. *Phys. Rev. B* **74**, 245413 (2006).
213. Wang, G. et al. Bending of multilayer van der Waals materials. *Phys. Rev. Lett.* **123**, 116101 (2019).
214. Lindahl, N. et al. Determination of the bending rigidity of graphene via electrostatic actuation of buckled membranes. *Nano Lett.* **12**, 3526–3531 (2012).
215. Poot, M. & van der Zant, H. S. J. Nanomechanical properties of few-layer graphene membranes. *Appl. Phys. Lett.* **92**, 063111 (2008).
216. Han, E. et al. Ultrasoft slip-mediated bending in few-layer graphene. *Nat. Mater.* **19**, 305–309 (2019).
217. Jiang, J.-W., Qi, Z., Park, H. S. & Rabczuk, T. Elastic bending modulus of single-layer molybdenum disulfide (MoS_2): finite thickness effect. *Nanotechnology* **24**, 435705 (2013).
218. Cunningham, G. et al. Solvent exfoliation of transition metal dichalcogenides: dispersibility of exfoliated nanosheets varies only weakly between compounds. *ACS Nano* **6**, 3468–3480 (2012).
219. Chiu, F. C. A review on conduction mechanisms in dielectric films. *Adv. Mater. Sci. Eng.* **2014**, 578168 (2014).
220. Quereda, J., Palacios, J. J., Agrait, N., Castellanos-Gomez, A. & Rubio-Bollinger, G. Strain engineering of Schottky barriers in single- and few-layer MoS_2 vertical devices. *2D Mater.* **4**, 021006 (2017).
221. Zeng, X., Hirwa, H., Metel, S., Nicolosi, V. & Wagner, V. Solution processed thin film transistor from liquid phase exfoliated MoS_2 flakes. *Solid State Electron.* **141**, 58–64 (2018).
222. Klein, C. A. & Straub, W. D. Carrier densities and mobilities in pyrolytic graphite. *Phys. Rev.* **123**, 1581–1583 (1961).

223. Barsoum, M. W. *MAX Phases: Properties of Machinable Ternary Carbides and Nitrides* (Wiley, 2013).
224. Kam, K.-K. *Electrical Properties of WSe_2, WS_2, $MoSe_2$, MoS_2, and Their Use as Photoanodes in a Semiconductor Liquid Junction Solar Cell*. Thesis, Iowa State Univ. (1982).
225. Morozov, S. V. et al. Giant intrinsic carrier mobilities in graphene and its bilayer. *Phys. Rev. Lett.* **100**, 016602 (2008).
226. Wang, M. C. et al. Unveiling electronic properties in metal-phthalocyanine-based pyrazine-linked conjugated two-dimensional covalent organic frameworks. *J. Am. Chem. Soc.* **141**, 16810–16816 (2019).
227. Wang, M. C. et al. High-mobility semiconducting two-dimensional conjugated covalent organic frameworks with *p*-type doping. *J. Am. Chem. Soc.* **142**, 21622–21627 (2020).
228. Kagan, C. R. Flexible colloidal nanocrystal electronics. *Chem. Soc. Rev.* **48**, 1626–1641 (2019).
229. Schiess, S. P. et al. Modeling carrier density dependent charge transport in semiconducting carbon nanotube networks. *Phys. Rev. Mater.* **1**, 046003 (2017).
230. Aigner, W. et al. Intra- and inter-nanocrystal charge transport in nanocrystal films. *Nanoscale* **10**, 8042–8057 (2018).
231. Kagan, C. R. & Murray, C. B. Charge transport in strongly coupled quantum dot solids. *Nat. Nanotechnol.* **10**, 1013–1026 (2015).
232. Lanigan, D. & Thimsen, E. Contact radius and the insulator–metal transition in films comprised of touching semiconductor nanocrystals. *ACS Nano* **10**, 6744–6752 (2016).
233. Baranovskii, S. & Rubel, O. in *Springer Handbook of Electronic and Photonic Materials* (eds Kasap, S. & Capper, P.) (Springer, 2017).
234. Bhaskaram, D. S. & Govindaraj, G. Carrier transport in reduced graphene oxide probed using Raman spectroscopy. *J. Phys. Chem. C* **122**, 10303–10308 (2018).
235. Blake, P. et al. Graphene-based liquid crystal device. *Nano Lett.* **8**, 1704–1708 (2008).
236. Muchharla, B., Narayanan, T. N., Balakrishnan, K., Ajayan, P. M. & Talapatra, S. Temperature dependent electrical transport of disordered reduced graphene oxide. *2D Mater.* **1**, 011008 (2014).
237. Seo, H. et al. Multi-resistive reduced graphene oxide diode with reversible surface electrochemical reaction induced carrier control. *Sci. Rep.* **4**, 5642 (2014).
238. Asada, Y., Nihey, F., Ohmori, S., Shinohara, H. & Saito, T. Diameter-dependent performance of single-walled carbon nanotube thin-film transistors. *Adv. Mater.* **23**, 4631 (2011).
239. Gao, J. & Loo, Y.-L. Temperature-dependent electrical transport in polymer-sorted semiconducting carbon nanotube networks. *Adv. Funct. Mater.* **25**, 105–110 (2015).
240. Nakamura, S., Ohishi, M., Shiraishi, M., Takenobu, T. & Iwasa, Y. Band structure modulation by carrier doping in random-network carbon nanotube transistors. *Appl. Phys. Lett.* **89**, 013112 (2006).
241. Li, Y., Paulsen, A., Yamada, I., Koide, Y. & Delaunay, J.-J. Bascule nanobridges self-assembled with ZnO nanowires as double Schottky barrier UV switches. *Nanotechnology* **21**, 295502 (2010).
242. Nguyen Minh, V., Kim, D. & Kim, H. Porous Au-embedded WO_3 nanowire structure for efficient detection of CH_4 and H_2S. *Sci. Rep.* **5**, 11040 (2015).
243. Reddy, K. M., Manorama, S. V. & Reddy, A. R. Bandgap studies on anatase titanium dioxide nanoparticles. *Mater. Chem. Phys.* **78**, 239–245 (2003).
244. Kumar, V., Sharma, M. K., Gaur, J. & Sharma, T. P. Polycrystalline ZnS thin films by screen printing method and its characterization. *Chalcogenide Lett.* **5**, 289–295 (2008).
245. Myung, Y., Wu, F., Banerjee, S., Park, J. & Banerjee, P. Electrical conductivity of p-type BiOCl nanosheets. *Chem. Commun.* **51**, 2629–2632 (2015).
246. Hanlon, D. et al. Liquid exfoliation of solvent-stabilized few-layer black phosphorus for applications beyond electronics. *Nat. Commun.* **6**, 8563 (2015).
247. Ippolito, S. et al. Covalently interconnected transition metal dichalcogenides networks via defect engineering for high-performance electronic devices. *Nat. Nanotechnol.* **16**, 592–598 (2021).
248. Hyun, W. J. et al. Scalable, self-aligned printing of flexible graphene micro-supercapacitors. *Adv. Energy Mater.* **7**, 1700285 (2017).
249. Majee, S., Song, M., Zhang, S.-L. & Zhang, Z.-B. Scalable inkjet printing of shear-exfoliated graphene transparent conductive films. *Carbon* **102**, 51–57 (2016).
250. Gao, Y., Shi, W., Wang, W., Leng, Y. & Zhao, Y. Inkjet printing patterns of highly conductive pristine graphene on flexible substrates. *Ind. Eng. Chem. Res.* **53**, 16777–16784 (2014).
251. Miao, F. et al. Inkjet printing of electrochemically-exfoliated graphene nano-platelets. *Synth. Met.* **220**, 318–322 (2016).
252. Michel, M., Biswas, C. & Kaul, A. B. High-performance ink-jet printed graphene resistors formed with environmentally-friendly surfactant-free inks for extreme thermal environments. *Appl. Mater. Today* **6**, 16–21 (2017).
253. Soots, R. A., Yakimchuk, E. A., Nebogatikova, N. A., Kotin, I. A. & Antonova, I. V. Graphene suspensions for 2D printing. *Tech. Phys. Lett.* **42**, 438–441 (2016).
254. Leng, T. et al. Graphene nanoflakes printed flexible meandered-line dipole antenna on paper substrate for low-cost RFID and sensing applications. *IEEE Antennas Wirel. Propag. Lett.* **15**, 1565–1568 (2016).
255. Huang, X. et al. Graphene radio frequency and microwave passive components for low cost wearable electronics. *2D Mater.* **3**, 025021 (2016).

Acknowledgements
The authors acknowledge the European Research Council Advanced Grant (FUTURE-PRINT) and the European Union under grant agreement no. 785219 Graphene Flagship Core 2. The authors have also received support from the Science Foundation Ireland (SFI) funded centre AMBER (SFI/12/RC/2278). The authors would also like to thank K. Stachura for preparing the graphics in Figs 2 and 6.

Author contributions
All authors researched data for the article; A.G.K. and J.N.C. discussed the content and wrote and edited the manuscript.

Competing interests
The authors declare no competing interests.

Peer review information
Nature Reviews Materials thanks Xiangfeng Duan and the other, anonymous, reviewer(s) for their contribution to the peer review of this work.

Publisher's note
Springer Nature remains neutral with regard to jurisdictional claims in published maps and institutional affiliations.

Supplementary information
The online version contains supplementary material available at https://doi.org/10.1038/s41578-021-00386-w.